Transient Fluid-Combustion Phenomena in a Model Scramjet

S. J. LAURENCE, S. KARL, J. MARTINEZ SCHRAMM AND K. HANNEMANN

Institute of Aerodynamics and Flow Technology, Spacecraft Department, German Aerospace Center, Bunsenstraße 10, 37073 Göttingen, Germany

(Received ?? and in revised form ??)

An experimental and numerical investigation of the unsteady phenomena induced in a hydrogen-fuelled scramjet combustor under high equivalence-ratio conditions is carried out, focusing on the processes leading up to unstart. The configuration for the study is the fuelled flowpath of the HyShot II flight experiment. Experiments are performed in the HEG reflected-shock wind tunnel, and results are compared with those obtained from unsteady numerical simulations. High-speed Schlieren and OH* chemiluminescence visualization, together with time-resolved surface pressure measurements, allow links to be drawn between the experimentally observed flow and combustion features. The transient flow structures signaling the onset of unstart are seen to take the form of an upstream-propagating shock train. Both the speed of propagation and the downstream location at which the shock train originates depend strongly on the equivalence ratio; however, the physical nature of the incipient shock system appears to be similar for different equivalence ratios. Both experiments and computations indicate that the primary mechanism responsible for the transient behaviour is thermal choking, though localised boundary-layer separation is observed to accompany the shock system as it moves upstream. In the numerical simulations, the global choking behavior is dictated by the limited region of maximum heat release near the shear layer between the injected hydrogen and the main flow: this leads to the idea of "local" thermal choking and results in a lower choking limit than suggested by a simple integral analysis. Such localised choking makes it possible for new quasi-steady flow topologies to arise, and these are observed in both experiments and simulation. Finally, a quasi-unsteady one-dimensional model is proposed to explain elements of the observed choking behaviour.

Key Words:

---

1. Introduction

Transient phenomena in scramjet engines are associated with such critical operational processes as dual-mode scramjet/ramjet transition and the onset of inlet unstart. The issue of unstart is a particularly important one. Defined as the upstream displacement or "disgorging" of the original inlet shock system (Heiser & Pratt 1994), unstart can cause violent and unsteady thermal and aerodynamic loads, even leading to the destruction of the engine; witness the recent failure of the second X-51 flight experiment. The causes of inlet unstart can be broadly divided into two groups: aerodynamic phenomena associated with the inlet flow itself, such as changes in Mach number or angle-of-attack, or boundary-layer separation on an intake surface; and processes that originate downstream in the

combustion chamber of the engine. The latter, involving complex interactions between flow and combustion features, are more difficult to study and form the focus of the present investigation. Thus, the term "unstart" is to be understood hereinafter as referring to the process whereby abnormal operating conditions in the combustion chamber generate upstream-propagating disturbances that subsequently affect the inlet flow.

Incipient unstart in scramjet engines is typically brought about through one of two processes, or a combination thereof: (1) excessive heat release in the combustion chamber leading to the flow reaching sonic conditions and thus becoming thermally choked; (2) the combustion-induced adverse pressure gradient causing the wall boundary layer(s) to separate, resulting in the formation of an oblique shock train which then propagates upstream. In the dual-mode ramjet/scramjet concept, this oblique shock train (or the normal shock train produced by thermal choking) may be captured by the isolator ahead of the combustor, but if the combustion-related pressure rise is too great, the shock train will continue moving upstream and unstart the inlet (Curran *et al.* 1996).

The transient flow phenomena associated with the onset of unstart have been the subject of a number of experimental investigations. In most of these, the combustion-induced pressure rise is replaced with mechanical throttling of the flow, for example, by pins (Wieting 1976), deflecting flaps (Rodi *et al.* 1996; Wagner *et al.* 2009) or plugs (Tan & Guo 2007; Tan *et al.* 2011), or through mass addition (Do *et al.* 2011); this allows the use of cold flows and the simpler implementation of diagnostic techniques. These studies have yielded information regarding the nature of unstart shock systems in isolators/inlets and the unsteady flow oscillations produced once full inlet unstart conditions are reached. However, such an approach is inadequate for gaining understanding of the interacting combustion/flow phenomena leading up to unstart in the combustion chamber itself.

In other studies, unstart has been induced by the injection of hydrogen at high equivalence ratios in model scramjet combustors. Shimura *et al.* (1998) carried out experiments on a large-scale scramjet engine attached to a force-measurement system. As the equivalence ratio, ϕ, was increased, pressure spikes were observed to develop with a frequency that increased with the strength of the subsequent unstart. Once unstart was established, violent oscillations in both the measured wall pressure and thrust were observed. The formation of an upstream-propagating separation bubble was postulated as the source of the pressure spikes, but the limited diagnostics employed meant that no further conclusions could be drawn. A study of a more fundamental nature was carried out by O'Byrne *et al.* (2000) in the T3 reflected-shock wind tunnel. Single-pass shadowgraphy and time-resolved pressure measurements were employed to investigate the thermal choking behaviour in a simple combustor, but again only limited information could be derived regarding the interaction between the combustion phenomena and the observed flow features. An additional source of uncertainty in these experiments was the high degree of driver-gas contamination often present during the choking process (up to approximately 60%).

Computational fluid dynamics (CFD) simulations potentially provide a valuable counterpart to experimental unstart investigations, as they afford a detailed picture of the three-dimensional combusting flow field. However, the chemically reacting nature of the flow, the uncertainty in turbulence models, and the strongly interacting viscous/inviscid flow features make even steady computations challenging. For time-resolved unsteady simulations, computational cost becomes a further issue. The difficulty of obtaining acceptable agreement between unsteady computations and experiments was demonstrated by the work of McDaniel & Edwards (1999, 2001), who carried out both two- and three-dimensional simulations of experiments performed in the Vitiated Air Generator (VAG) of the Japanese National Aerospace Laboratory (Boyce *et al.* 2000). At a high equivalence

ratio ($\phi = 0.61$), experimental choking was observed; consistent transient behaviour developed in the simulations, with massive combustion-induced separation leading to rapid unstart. However, at a lower equivalence ratio ($\phi = 0.29$), three-dimensional simulations showed a slow progression to unstart, in contrast to the stable combustion observed in both experiments and two-dimensional simulations. Questions remained concerning the grid resolution, the combustion model and the choice of boundary conditions.

In the present study, the transient flow and combustion features produced by the injection of hydrogen at high equivalence ratios in a scramjet combustor are investigated experimentally in a wind-tunnel reproduction of the HyShot II flight configuration. The diagnostic tools employed - time-resolved surface pressure measurements, and high-speed Schlieren and OH* chemiluminescence visualizations - allow an unprecedented level of insight into the interacting fluid and combustion phenomena. Unsteady numerical simulations are employed alongside the experiments to provide detailed information regarding the mechanisms responsible for the transient behaviour. The layout of this paper is as follows. The experimental and numerical methodologies are described in § 2 and § 3, respectively. A brief discussion of stable combustion results appears in § 4, and in § 5, experimental and computational results pertaining to the unsteady phenomena leading up to unstart are presented. In § 6, we describe experimental measurements made under full unstart conditions. A discussion of the salient points follows in § 7, and in § 8, a simple one-dimensional quasi-unsteady model is proposed to explain elements of the observed transient behaviour. Conclusions are drawn in § 9.

2. Experimental methodology

2.1. *Facility and test conditions*

All experiments were carried out in the HEG (High Enthalpy shock tunnel, Göttingen) facility of the German Aerospace Center (DLR). The HEG is a reflected-shock wind tunnel, capable of producing flows over a wide range of stagnation pressures and total enthalpies. Further information on the operating principles and the test conditions achievable in HEG is provided in Hannemann (2003). Briefly, to initiate a test run, compressed air is used to accelerate a free piston down a compression tube filled with a mixture of helium and argon. A primary diaphragm initially separates the compression tube from the shock tube containing the test gas, in this case air. When the pressure in front of the piston reaches a sufficiently high level, the diaphragm bursts, sending a strong shock wave down the shock tube. This shock reflects from the far end of the shock tube, rupturing the secondary (mylar) diaphragm, which until this instant separates the evacuated tunnel nozzle and test section from the shock tube. The reflected shock also decelerates the test gas in the shock tube to stagnation conditions, forming a reservoir for the subsequent expansion through the hypersonic nozzle and into the test section. Quasi-steady test conditions typically persist for several milliseconds; the test time is terminated either by the arrival of the expansion wave from the primary diaphragm burst or by contamination of the test flow by the driver (compression tube) gas.

For all tests in the current investigation, HEG Condition XIII (p_0=17 MPa, h_0=3.4 MJ/kg), designed to simulate the flight conditions of the HyShot II vehicle at 28 km altitude, was employed. The free-stream properties corresponding to these stagnation conditions have been calculated computationally (and compared with extensive calibration measurements) as M=7.4, T=270 K, and ρ=0.026 kg/m^3. In figure 1 are shown reservoir, Pitot and static pressure measurements (the latter two scaled to allow a direct comparison) from a typical experiment in the present study. The point t=0 corresponds to the instant

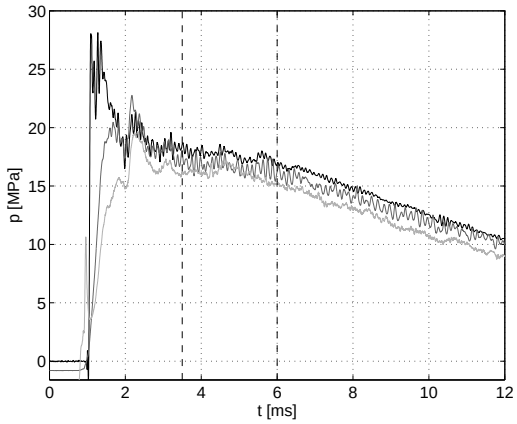

FIGURE 1. Measured reservoir (dark), free-stream Pitot (medium), and free-stream static (light) pressure traces for the test condition used in the present experiments. The time-scale of the reservoir trace has been shifted to account for the passage of the flow through the nozzle, and the free-stream traces have been vertically scaled and shifted to allow convenient comparison. The quasi-steady test time is indicated by vertical dashed lines.

of shock reflection from the shock-tube end wall; this convention is used throughout this paper. The time-scale of the reservoir trace has been shifted to account for the passage of the flow through the nozzle. The quasi-steady test time, from 3.5 to 6.0 ms, is indicated by dashed vertical lines. This was the typical test duration chosen for steady combustion experiments; however, the flow is established and has achieved roughly constant conditions by 2.5 ms. This latter point will be important in the results discussed in § 5, as in some cases the transient phenomena under investigation were observed to be initiated before the beginning of the nominal test period.

Previous investigations have shown that a comparison of the static pressure development with that of the reservoir and Pitot pressures gives a good indication of the onset of driver-gas contamination (Hannemann *et al.* 2000): the Pitot pressure is typically unaffected by the arrival of driver gas in the free stream and continues to follow the reservoir pressure, but the static pressure drops more rapidly once driver gas is present. In figure 1, we note that the static pressure development follows that of the reservoir and Pitot pressures until at least 12 ms, indicating that there is no significant contamination during this time. The steady test time is instead terminated by the arrival of the expansion wave from the primary-diaphragm burst.

2.2. *Model configuration*

The experimental model used for this investigation was a 1:1-scale reproduction of the fuelled flow path of the HyShot II flight experiment. HyShot II was the first successful flight in the HyShot program of the University of Queensland, designed to provide benchmark supersonic combustion data at a flight Mach number of approximately M=8 (Smart *et al.* 2006). Extensive ground-testing of the HyShot II configuration has already been carried out, both at the University of Queensland (Smart *et al.* 2006; Frost *et al.* 2009) and in HEG (Gardner *et al.* 2004; Hannemann *et al.* 2008, 2010), and its simple combustion chamber design, allowing for convenient optical access, made it a suitable choice for the present study. The basic model configuration was as tested in the previous HEG experiments just referred to, but modifications were made to improve handling and optical access. A schematic of the model and a cut through the internal geometry are shown in figure 2 (note that the orientation in the latter is upside-down relative to the physically

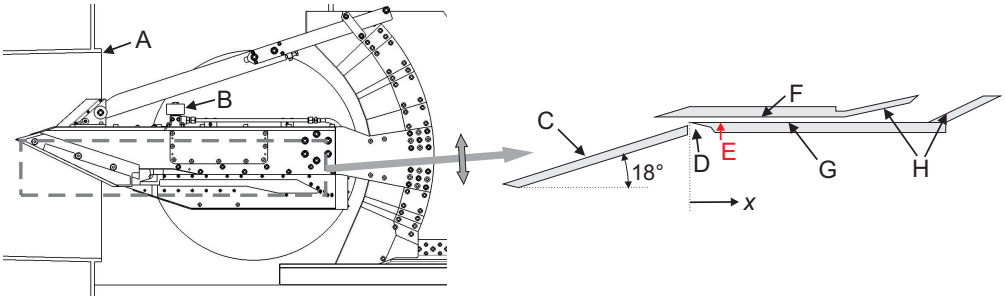

FIGURE 2. (Left) Schematic showing the HyShot II model in the HEG test section: (A) HEG nozzle; (B) H_2 injection valve. (Right) Schematic of the fuelled flow-path of the HyShot II model (upside-down relative to the left schematic): (C) intake ramp; (D) boundary-layer bleed channel; (E) injection location; (F) cowl-side wall; (G) injector-side wall; (H) exhaust surfaces. The origin of the x-coordinate system used throughout this article is the leading edge of the injector-side wall.

tested configuration; to be consistent with previously presented results, this upside-down orientation is used throughout this work).

The model intake is a simple wedge of half-angle 18°, equipped with sidewalls to ensure the two-dimensionality of the flow at the combustion chamber entrance. To prevent the intake-ramp boundary layer from entering the combustion chamber, a bleed channel is situated between the intake and the combustor entrance; this also serves to swallow the shock generated at the leading edge of the cowl. The combustion chamber is a constant-area duct of 300 mm length, with a rectangular cross-section of 75×9.8 mm. The constant-area section is followed by a simple two-dimensional expansion formed by two exhaust-surface plates. For all experiments described herein, the model was mounted at an angle-of-attack of 3.6°, i.e., the intake ramp formed an angle of 21.6° to the free stream. The average flow conditions at the entrance to the combustor were computed as M=2.49, T=1380 K and p=130 kPa (see the following section).

Hydrogen fuel was injected in the wall-normal direction through four evenly spaced port-holes on the intake-ramp-side wall of the combustion chamber (hereinafter referred to as the injector-side wall) at a distance 58 mm downstream from the wall leading edge. The injection port-holes were each of radius 1 mm, providing a total injection area of 12.6 mm^2. The hydrogen was supplied via a Ludwieg tube, capable of providing an approximately constant pulse of fuel for 50 ms at fill pressures of up to 15 MPa, though the maximum pressure used in the present experiments was 2.2 MPa. To ensure the hydrogen flow was fully established by the arrival of the test gas, injection was initiated by opening a fast-acting solenoid valve approximately 20 ms before the test time.

2.3. *Measurement techniques*

The model was heavily instrumented with both pressure transducers and thermocouples for heat-flux measurements, but the latter will not be discussed in the present work. In total, 57 pressure transducers were distributed over the inlet ramp, the combustion chamber walls and the exhaust surfaces; the model was also equipped with probes to measure the free-stream Pitot and static pressures, and a reference heat-flux value. In the combustion chamber, a single row of pressure transducers was installed on each of the injector- and cowl-side walls along the model plane-of-symmetry, lying midway between two injection port-holes. The transducer type employed was the Kulite XCEL-100, with a maximum pressure range, depending on the particular transducer, of between 170 and 700 kPa and a resonant frequency above 150 kHz.

One of the main focuses of the current experiments was the determination of the approximate flame location in the combustion chamber through visualization of OH* chemiluminescence. OH* chemiluminescence intensity, being a line-of-sight quantity, is limited in its ability to provide quantitative results when measured in three-dimensional flow-fields; nevertheless, it gives a reliable indication of the global onset of combustion and has been recommended as an attractive option even for more complex hydrocarbon flames where other, especially laser-based, techniques would be difficult to apply (Haber & Vandsburger 2003). It is also suitable for the high-speed visualization necessary to investigate the unsteady phenomena that are of interest in the present study. The OH* visualization apparatus consisted of a Shimadzu HPV-1 high-speed camera together with a LaVision HS-IRO intensifier. Both the model combustor sidewall and the HEG test section were fitted with quartz windows to allow transmittance of the relevant wavelengths ($\sim$310 nm), and a custom band-pass filter (of 50 nm width centered at 310 nm) was placed in front of the intensifier to block both other flame emissions and the self-luminosity produced by the facility. For steady combustion tests (ϕ=0.35), images were captured at 8 kfps with an integration time of 60 μs; for higher equivalence ratios, the more intense combustion allowed a shorter exposure time of 10 μs combined with a camera frame rate of 16 kfps.

High-speed Schlieren imaging was also employed to visualize the flow structures within the combustion chamber. The light source was a Cavilux Smart pulsed-diode laser, a device that produces light pulses at 690 nm with high repetition rates and durations as short as 10 ns. The short pulse duration effectively freezes the visualized flow structures, while the use of monochromatic light allows extraneous luminosity to be removed with a bandpass filter. An additional advantage of this device is that the beam is effectively incoherent, eliminating the diffraction effects usually associated with laser light sources (Settles 2006). A conventional Z-fold Schlieren setup with a horizontal knife-edge was employed, with images recorded by the Shimadzu HPV-1 camera. Typical frame rates were 16 or 32 kHz, and light pulses of 30 ns duration were used. Since only a single high-speed camera was available, OH* and Schlieren images could not be obtained simultaneously. Also, the limited pixel-count of the Shimadzu camera (312$\times$260 pixels) meant that, in order to provide acceptable resolution across the duct height, only approximately one third of the duct length could be visualized in a given experiment.

3. Computational methodology

3.1. *Numerical model*

All numerical simulations in the present study were performed with the hybrid structured/unstructured DLR Navier-Stokes solver TAU (Gerhold *et al.* 1997). The TAU code is a second-order finite-volume flow solver for the Euler and Navier-Stokes equations in their integral forms, using eddy-viscosity, Reynolds-stress or detached- and large eddy simulation for turbulence modeling. It has been validated for a wide range of steady and unsteady subsonic, transonic and hypersonic flows. For the present investigation, the Spalart-Allmaras one-equation eddy viscosity model was employed; the AUSMDV flux-vector splitting scheme was applied together with MUSCL gradient reconstruction to achieve second-order spatial accuracy. In unsteady computations, the dual time-stepping technique described by Jameson (1991) was employed.

The combustion model in the TAU code is an extension of the chemical and thermal nonequilibrium models used to simulate high-enthalpy re-entry flows. The fluid is considered to be a reacting mixture of thermally perfect gases, with a transport equation

solved for each of the individual species. The chemical source terms in this set of transport equations are computed from the law of mass action by summation over all participating reactions. The forward reaction rate is computed using the modified Arrhenius law, and the backward rate is obtained from the equilibrium constant which is derived directly from the partition functions of the participating species. A modified Jachimowski reaction mechanism for hydrogen-air mixtures, as described by Gerlinger (2001), was applied for this investigation. This mechanism includes both hydrogen peroxide (H_2O_2) and the perhydroxyl radical (HO_2) and is valid over a wide range of pressures, densities and equivalence ratios.

The thermodynamic properties (energy, entropy, specific heat) are calculated using the partition functions for each individual species in the reacting gas mixture. Knowledge of the mixture composition and the thermodynamic state of the individual species allows the properties of the reacting gas mixture to be computed using suitable mixture rules, such as those proposed by Wilke (1950) for viscosity and by Herning & Zipperer (1936) for heat conductivity. A non-catalytic wall boundary condition, i.e., a von Neumann condition, is used for the species partial densities. The species diffusion fluxes are modeled using Ficks law, applying an averaged diffusion coefficient for all species. The approximate diffusion coefficient thus derived is computed using the laminar and eddy viscosities, and constant Schmidt numbers (laminar and turbulent) of 0.7. Dedicated modeling of turbulence-chemistry interactions is neglected in this study.

3.2. *Computational domains and boundary conditions*

The CFD analysis of the HyShot II configuration was split into a two-dimensional simulation of the intake flow and a three-dimensional analysis of the combustor flow. For the latter, simulation of the entire combustor would result in a prohibitive computational cost; thus, the symmetries of the geometry were exploited, and only a slice covering one-eighth of the physical domain was considered, with symmetry conditions applied at the spanwise boundaries. The free-stream conditions for the intake computation were assumed to be constant in space and were obtained by averaging the results of an HEG nozzle-flow simulation employing the approximate reservoir conditions used in the present study. Karl & Hannemann (2008) and Hannemann *et al.* (2010) provide further details of this methodology.

For the combustor section, the flow profile obtained from the intake analysis was prescribed as a Dirichlet boundary condition at the inflow plane located 5 mm downstream from the leading edge of the injector-side wall. The outflow plane was located at x=410 mm, i.e., 110 mm of the exhaust expansion were included. The boundary condition applied at this plane was an upwind-flux-based pressure outlet, consisting of a simple extrapolation of the conservative variables in the supersonic flow region and a prescription of the exit pressure (i.e., the test-section back pressure) in subsonic flow regions. Symmetry boundary conditions were applied at the spanwise boundary planes: one located along a cut through the center of an injection port-hole, the other on the plane midway between two port-holes. The bottom and top walls were modelled with a viscous no-slip boundary condition, for which the wall temperature was fixed at 300 K to account for the short test time in HEG. Transition from laminar to turbulent flow in the wall boundary layers was set according to a criterion based on Re_θ, the momentum-thickness Reynolds number, as Re_θ/M_e=200, where M_e is the Mach number at the boundary-layer edge (Bertin *et al.* 1997). The suitability of this criterion was supported by surface heat-flux measurements inside the combustor.

The hydrogen injection was modelled by partially including the injector in the computational domain. A reservoir inflow condition was applied at the hydrogen inflow bound-

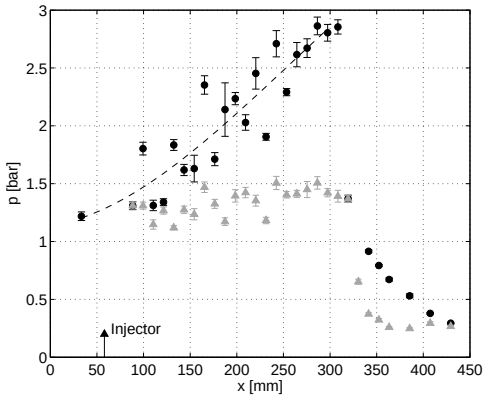

FIGURE 3. Mean pressure profiles on the injector-side wall of the HyShot II combustor for fuel-off conditions (△) and for an equivalence ratio of 0.35 (○). The dashed line indicates the fuel-on trend within the constant area section of the combustion chamber (x=0-300 mm).

ary: the thermodynamic conditions were computed using an isentropic expansion from prescribed stagnation conditions using the inflow velocity vector, obtained as part of the CFD solution. The computational grid covering the combustor domain consisted of approximately 1 million cells. Structured prismatic sublayers were used at the viscous walls; a dimensionless wall spacing of y^+=$O(1)$ ensured sufficient resolution for the low-Reynolds-number turbulence model and for computation of the wall heat flux. Further information regarding the computational methodology can be found in Karl (2011).

4. Stable combustion

In order to provide a context for the unsteady combustion results to be discussed in the following section, we begin by briefly outlining results from experiments and computations in which steady combustion developed within the combustor.

4.1. *Experimental results*

Stable combustion was obtained in experiments by limiting the equivalence ratio to 0.35. In figure 3 is shown the pressure distribution along the injector-side wall, averaged over the test time, in one such experiment; this is compared with equivalent fuel-off measurements. The error bars in each case indicate the variation in pressure during the test time. Within the constant-area section of the combustor (x=0-300 mm), a gradual rise in the pressure level (as indicated by the dashed trend line) is clearly visible in the fuel-on profile, in contrast to the approximately constant pressure for the fuel-off case. This fuel-on profile, lacking the characteristic pressure plateaus typically associated with boundary-layer separation in a constant-area duct (Curran *et al.* 1996), is indicative of "clean" supersonic combustion. There are significant fluctuations superimposed upon the general upward trend: these are produced by reflections of the injection-generated shock propagating down the duct, which generates sharp variations in the local pressure. In the diverging section of the geometry (x>300 mm), a steep drop in the static pressure is observed.

In figure 4 are shown Schlieren and false-colour OH* chemiluminescence visualizations of the section of the combustion chamber immediately downstream of injection (56 to 136 mm). The point of injection is at the lower left corner of each image. To improve the signal-to-noise ratio, the OH* image has been averaged over several visualizations

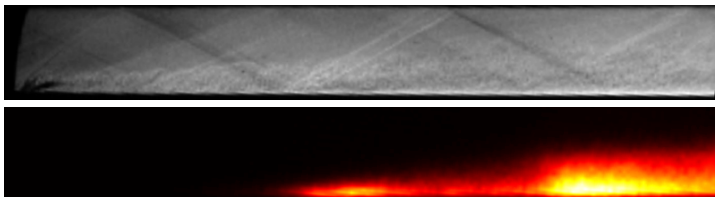

FIGURE 4. Schlieren (above) and false-colour OH* chemiluminescence (below) visualizations of the flow downstream of the injector (x=56-136 mm) for an equivalence ratio of 0.35.

recorded during the steady test time. The barrel shock generated by the hydrogen injection is clearly seen in the Schlieren image, together with several of its reflections extending down the duct. The hydrogen jet itself is also visible: the freezing of the turbulent structures enabled by the short pulse duration of the light source is shown to good effect here. The injected hydrogen appears to have penetrated to approximately half the duct height by the downstream end of the visualized section. The OH* visualization shows the onset of combustion to be clearly linked to the shock structure in the duct: in particular, the first reflection of the injection shock appears to initiate combustion close to the injector-side wall; the second reflection then "kicks" the flame further out into the duct and increases the intensity of combustion.

4.2. *Analysis of operational limits*

In order to investigate the response of the HyShot II combustor to variations in the equivalence ratio, and in particular, to identify the operational limits of the "clean" supersonic combustion mode, steady numerical simulations were carried out using various pressures in the hydrogen injector plenum while keeping the inlet conditions constant. The plenum pressure was increased from 3 bar to 8 bar in steps of 1 bar, resulting in equivalence ratios from 0.14 to 0.47.

In figure 5 we show pressure distributions on the injector-side combustor wall for the different equivalence ratios. The general trend is for the overall pressure rise to increase for higher equivalence ratios, as the additional available fuel leads to a greater heat release. No converged CFD solution could be obtained for the largest equivalence ratio considered of 0.47 (the dashed pressure distribution in figure 5), as in this case, a separated flow region developed on the injector-side wall and subsequently moved upstream, causing strong oscillations in the flow field and preventing the CFD solution from converging to a steady state.

As described in § 1, the two general operational limits which can lead to choking of the combustor flow and potentially to unstart of scramjet engines are thermal choking and boundary-layer separation. An integral thermal choking limit was estimated for the present combustor entrance conditions using a control-volume analysis, assuming ideal equilibrium combustion; approximations for the skin friction and heat loss through the cold combustor walls, calculated from the CFD solutions, were included. According to this analysis, thermal choking occurs at an equivalence ratio of 0.49, corresponding to a combustor pressure rise of p/p_i=3.81, where p_i is the pressure at the inlet. This estimate does not include the pressure rise from the hydrogen injection and assumes the heat addition to take place uniformly over the duct cross-section. Note that only the choking equivalence ratio, and not the corresponding pressure rise, relies on the assumption here of complete combustion.

Limits for the shock-induced separation of turbulent boundary layers have been proposed by several researchers, for example, Love (1955) and Korkegi (1975). Frost *et al.*

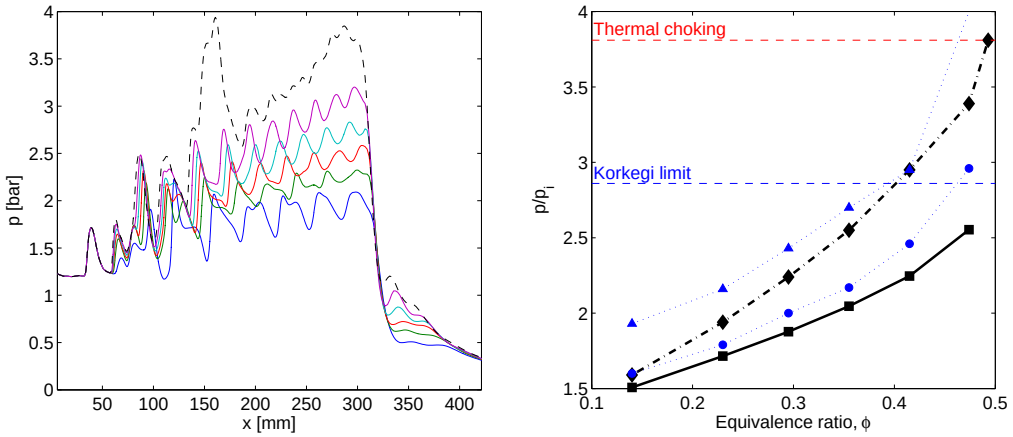

FIGURE 5. (Left) Computed surface pressure distributions on the injector-side wall for equivalence ratios of (solid lines, minimum to maximum levels) 0.140, 0.230, 0.295, 0.355 and 0.415, and (dashed) 0.474. (Right) Combustor pressure ratios obtained from stream-thrust averaging the computational results (□) and an equilibrium control-volume analysis (◇), together with maximum computed pressures on both the injector-side (○) and cowl-side (△) walls, all as functions of the computational equivalence ratio. Also shown are the estimated critical pressure ratios for thermal choking and boundary-layer separation.

(2009) suggested that the Korkegi criterion can also be applied to the more gradual pressure rises experienced in scramjet combustors; in this case, the critical pressure ratio at which flow separation occurs is given by

$$p/p_i = \begin{cases} 1 + 0.3M_i^2 & \text{for } M_i \leqslant 4.5, \\ 0.17M_i^{2.5} & \text{for } M_i > 4.5, \end{cases} \tag{4.1}$$

where M_i is the inlet Mach number. For the present configuration, this gives a critical pressure ratio of 2.9. Heiser & Pratt (1994) cite the Love criterion, $M/M_i < 0.762$, for illustration, without recommending its use for design purposes; for the HyShot II combustor entrance conditions, it predicts an earlier onset of separation than the Korkegi criterion. In either case, we are led to the same conclusion as Frost *et al.* (2009): that choking of the HyShot II combustor should be initiated by boundary-layer separation rather than thermal choking. This conclusion is also consistent with the qualitative combustion behavior in the steady computations just discussed.

An analysis of the steady computational results was performed in order to determine where the combustor flow conditions lay relative to these limits at the various equivalence ratios. The pressure rise was calculated in each case using a stream-thrust averaging approach. In addition, a theoretical equilibrium pressure rise was calculated using a control-volume analysis, assuming complete combustion and including estimates of frictional and heat-loss effects from the computations (as just described for the calculation of the thermal choking limit). These results are plotted in the right part of figure 5 together with the thermal choking and Korkegi limits; also shown are the peak pressures on the injector- and cowl-side walls in each numerical simulation. It is immediately apparent that the equilibrium analysis significantly overestimates the average pressure rise in the combustion chamber for all but the lowest equivalence ratio. This is because, contrary to the assumption of complete combustion independent of the equivalence ratio, the combustion efficiency decreases markedly with increasing ϕ: the amount of unburned hydrogen at the combustor exit increases from 7.8% for ϕ=0.14 to 26% for ϕ=0.41. Thus, while the control volume analysis predicts the onset of thermal choking at approximately

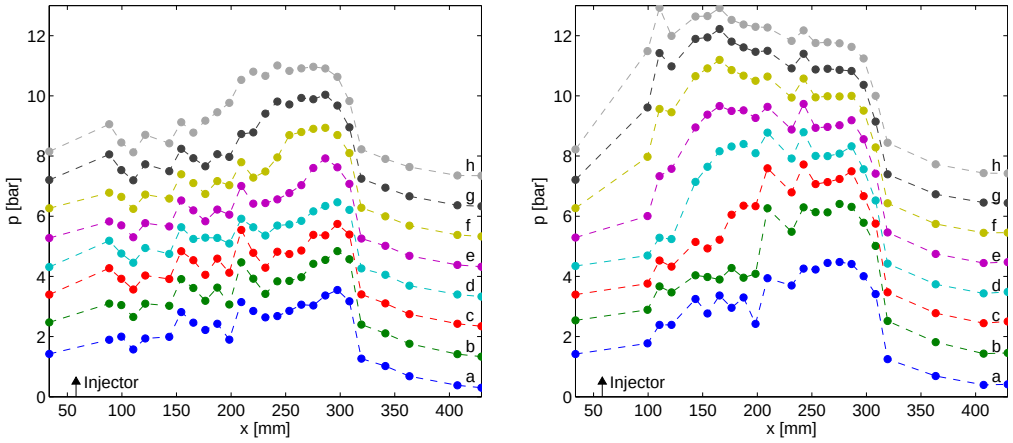

FIGURE 6. Unsteady experimental pressure development inside the combustion chamber for equivalence ratios of (left) 0.5 and (right) 0.7. The measurements are made on the injector-side wall, and are at times (a) 2.4, (b) 2.6, (c) 3.0, (d) 3.4, (e) 3.8, (f) 5.2, (g) 5.6, and (h) 6.6 ms. For clarity, all traces except the first in each plot have been shifted upwards by an integral number of bars.

ϕ=0.5, the stream-thrust-averaged profile is still well below the critical pressure ratio at which this would occur. Moreover, the latter profile is still below the Korkegi limit at the highest ϕ considered, although the local maximum pressures on both the injector- and cowl-side walls have exceeded this value. In fact, the Korkegi limit applied to the injector-side wall appears to give a good indication of the onset of separation in the steady-state computations. That separation occurs first on the injector-side wall rather than on the cowl-side wall, despite the higher maximum pressure on the latter, is likely due to the fact that the peak pressure on the cowl-side wall occurs at the first impingement location of the injector barrel shock and is followed by an expansion that rapidly decreases the pressure and re-stabilizes the boundary layer. On the injector-side wall, the boundary layer has already been disturbed by the injected hydrogen and thus is more prone to separation.

5. Unsteady combustion

5.1. *Experimental results*

In previous experimental studies involving the HyShot II configuration (Frost *et al.* 2009; Hannemann *et al.* 2008), choking of the combustor was found to occur as the equivalence ratio was increased above a value of approximately 0.5. The onset of choking took the form of a pressure disturbance that developed in the rear of the combustor and began to propagate upstream. Based on a simple Rayleigh-flow analysis, Frost *et al.* (2009) ruled out thermal choking as a possible source of the choking behaviour, and boundary-layer separation was assumed to be responsible.

Similar unsteady choking behaviour was noted in the present experiments. Figure 6 shows examples for equivalence ratios of 0.5 and 0.7: in each case, the pressure distribution on the injector-side wall is shown at various times in the relevant experiment. For ϕ=0.5, a relatively steady pressure rise initially extends down the duct (t=2.4 ms), reaching a level slightly exceeding the maximum pressure for ϕ=0.35. This pressure rise subsequently steepens towards the rear of the combustor and, from around t=3.8 ms, begins to propagate upstream. By the latest time shown (t=6.6 ms), the onset of the

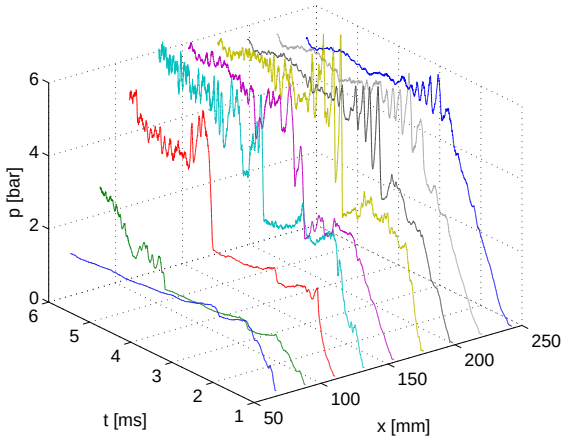

FIGURE 7. Time-resolved pressure traces at various positions on the cowl-side combustor wall for an equivalence ratio of 0.7.

pressure rise has reached approximately the midpoint of the duct, $x{\approx}170$ mm. For ϕ=0.7, the unsteady behaviour is similar, but happens on a much-compressed timescale and involves higher pressures. The initial profile shows a somewhat steeper rise than in the lower equivalence ratio case, plateauing close to x=250 mm at a level almost three times the duct-entrance pressure. This pressure rise steepens further and begins to propagate up the duct almost immediately. By the end of the test time (∼6 ms), a sharp pressure jump has developed immediately downstream of the injection location, followed by an extended plateau region. At t=6.6 ms, however, the pressure rise has still not reached the transducer at 44 mm, upstream of the injection port-holes.

5.1.1. *ϕ=0.7*

We concentrate first on the experimental results for ϕ=0.7, as the largest amount of data was gathered at this equivalence ratio. In order to further elucidate the behaviour of the transient system responsible for the time-developing pressure profiles in the right part of figure 6, in figure 7 are plotted time-resolved pressure traces at various positions on the cowl-side wall for the same experiment. Following the initial pressure rise signalling the arrival of the test flow, strongly oscillatory signals are visible at the downstream pressure stations, with the amplitude of the oscillations reaching a maximum near x=176 mm. This suggests the development of moving periodic flow structures, in particular, the propagation of an unsteady shock train up the combustor. Upstream of x=176 mm, however, the periodic structures become progressively less well defined and eventually form just a single sharp rise followed by residual unsteadiness. This behaviour is indicative of a breakdown in the shock train structure.

In figure 8 are plotted x-t diagrams showing the motion of the leading edge of the shock system on both the injector- and cowl-side walls, as determined by the arrival of the corresponding pressure rise at each transducer. Results from all experiments with an equivalence ratio of 0.7 (±0.04) are shown. In all cases, the upstream motion begins before the nominal start of the steady test time (3.5 ms), but as noted earlier, the test flow may be considered to be approximately steady by 2.5 ms. The speed of propagation is seen to be approximately constant between $x \approx 200$ and 120 mm, with a slight upward concavity indicating that the system is gradually slowing as it moves forward. From $x \approx 120$ mm this slowing becomes more pronounced and is typically followed by a pause in the upstream motion somewhere between 44 and 84 mm (this is most clearly seen in

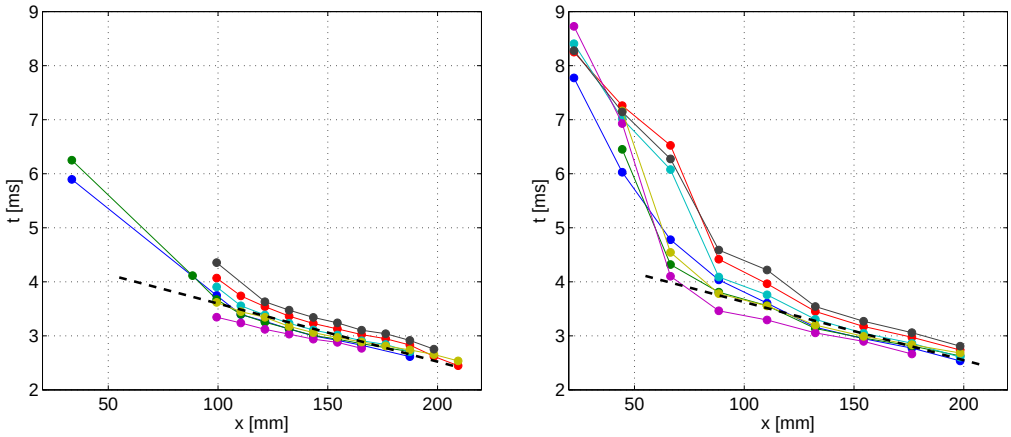

FIGURE 8. X-t diagrams showing the motion of the leading edge of the unsteady shock train in the combustor for an equivalence ratio of 0.7: (left) injector-side wall; (right) cowl-side wall. The dashed line in each case indicates a propagation speed of 93 m/s.

the cowl-side traces). Following the conclusion of the test time (6 ms), the shock system continues to move upstream of the injector at a speed significantly below that with which it propagated downstream of injection. It should be noted here that the injection pressure remains approximately constant for some 25 ms after the end of the test time, whereas the reservoir pressure decreases monotonically during this period (see figure 1), thus leading to a continual increase in the effective equivalence ratio. In each of the plots in figure 8, a line is shown with a slope corresponding to a propagation speed of 93 m/s, and this matches well with the speed of the system in the initial part of its upstream motion.

We now turn to the high-speed Schlieren and OH* visualizations recorded during this period of unsteady development. Correlating the flow and combustion features visualized using the two techniques was complicated by the fact that, as mentioned in § 2.3, only one or the other could be applied in a given experiment; however, by comparing the shock-train motions plotted in figure 8, the effective time-offset between pairs of experiments could be determined. It should be kept in mind in interpreting these images that both techniques are line-of-sight, and that the flow-field is highly three-dimensional.

In figure 9 are shown sequences of Schlieren and OH* visualizations of flow regions immediately downstream of the injector (x=56-136 mm) and in the central combustion chamber (x=158-228 mm). Concentrating first on the sequence near the injector, the picture is initially similar to that for ϕ=0.35, except with a higher degree of injectant penetration and stronger injection-related shocks due to the increased mass flow of hydrogen. Weak combustion is again visible in the OH* image in regions close to the injector-side wall where reflections of the injection barrel-shock impinge on the hydrogen jet (note the exposure time here is significantly shorter than in figure 4). By t=3.5 ms, the arrival of the upstream-propagating shock system is visible in the Schlieren image. Corresponding to this, a bulging structure appears in the OH* visualization, slightly preceding the shock visible on the cowl-side wall. This structure suggests the development of boundary-layer separation on the injector-side wall, since the increased residence time in a separated flow region will enhance ignition and lead to increased levels of OH* production. The appearance of the unsteady flow structures in the lower part of the combustor in this and the following Schlieren visualizations is also consistent with separation of the injector-side-wall boundary layer.

The shock train continues to propagate upstream until approximately 4.4 ms, but there-

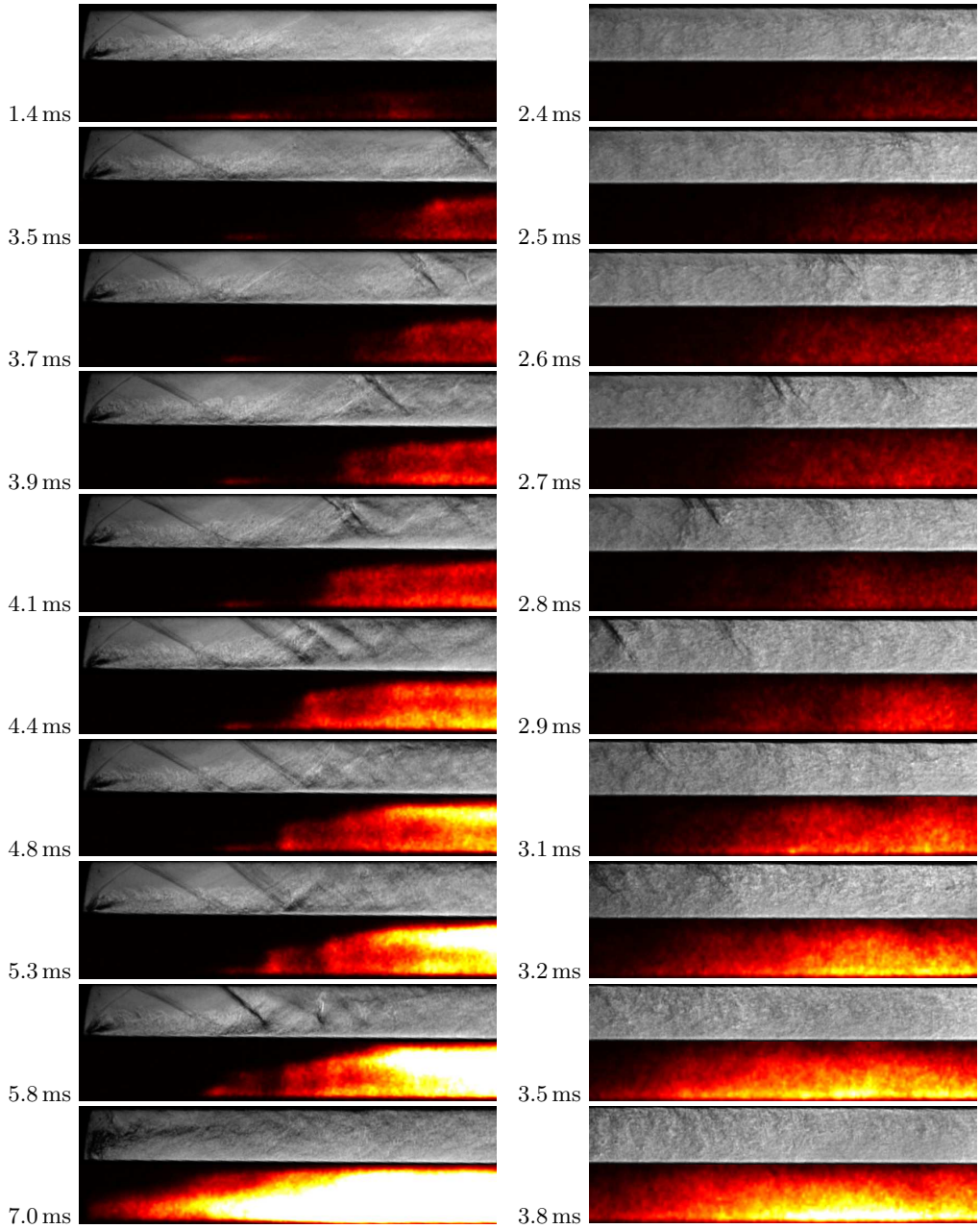

FIGURE 9. Sequences of quasi-synchronous Schlieren and OH* chemiluminescence images of the flow (left) near the injector (x=56-136 mm) and (right) in the central combustion chamber (x=158-228 mm) for an equivalence ratio of 0.7.

after the combustor flow appears to find a quasi-stable configuration, with an oblique shock lodged on the cowl-side wall approximately 3 duct heights downstream of the injector. The main combustion region then begins immediately downstream of the impingement location of this shock on the injector-side wall; unsteady flow structures, suggesting the presence of large-scale flow separation in this region, are observed in the Schlieren images. Because of the limited test time, it is difficult to conclude whether this

configuration is truly stable or simply a transient quasi-stable flow topology. Following the conclusion of the test time (6.0 ms), the shock system continues moving upstream past the injection point; however, it is not clear whether this is due entirely to the increasing effective equivalence ratio or, if given sufficient time at a constant equivalence ratio, whether such behaviour would develop regardless. Comparing the Schlieren and OH* images from 4.4 to 5.3 ms, it is apparent that, although the position of the cowl-side shock is relatively fixed, the combustion downstream is intensifying, which in itself could eventually lead to further upstream propagation of the shock-train. Such quasi-stable shock propagation behaviour has been noted previously, for example, by Do *et al.* (2011) during duct experiments in which choking was induced by mass addition.

Having examined the transient shock system as it approaches the injection location, we now look to the origin of this system in the central combustion chamber, seen in the sequence in the right part of figure 9. As suggested by the pressure traces in figure 7, the nascent system takes the form of an unsteady shock train that propagates up the duct (t=2.6 to 3.1 ms). The individual structures in this shock train are most visible on the cowl-side wall, probably because the lateral extent of the supersonic flow region is greatest in this part of the combustor, but it is apparent in several of the Schlieren images (e.g., that at 2.8 ms) that parts of the shock system extend over the height of the duct. The appearance of the system is quite different from that of the canonical bifurcated shock train associated with shock/boundary-layer interactions in internal geometries (Matsuo *et al.* 1999), and this is no doubt partly due to the highly three-dimensional nature of the flow. However, the trailing cowl-side shocks in the train do not appear to be significantly displaced from the wall, which would be expected if boundary-layer separation were playing a crucial role here. Moreover, in comparing the Schlieren and OH* images, we note that, although the onset of the shock system appears to be related to the intensification of combustion within the duct, there are no strong combustion features that follow the movement of the shock train upstream. In particular, if separation of the boundary-layer were driving the shock system up the combustor, we would expect the separated regions to be visible as strong features moving upstream in the OH* images, as already seen in the previous visualization sequence. The fact that no such features are observed here suggests that the primary mechanism driving the development of the transient shock system is thermal choking, rather than boundary-layer separation. Following the propagation of the shock train out of the visualization window, steadily increasing levels of OH* are observed, indicating that the combustion is continuing to intensify. The apparent absence of upstream-propagating boundary-layer separation in this sequence suggests that the onset of the separation bubble presumed to be present in the upstream sequence likely occurred in the region between the two visualization windows, i.e., between 136 and 158 mm.

5.1.2. *ϕ=0.5*

Two experiments were performed with equivalence ratios of approximately 0.5; in figure 10 we show time-resolved pressure traces on the cowl-side wall from one of these. The development of the oscillatory pressure signals towards the rear of the combustion chamber is similar to that of the ϕ=0.7 case shown in figure 7, again indicating the formation of an upstream-propagating shock train; however, now the periodic structures are already well-developed at the most downstream point shown (x=242 mm), indicating that the shock train has originated from further down the combustor. The speed of propagation is also slower: a value of approximately 31 m/s was estimated from x-t diagrams. Again, a breakdown of the periodic structures is observed, here between approximately 176 and 154 mm.

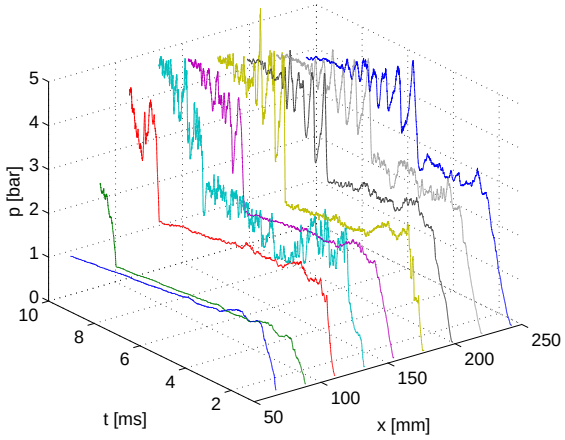

FIGURE 10. Time-resolved pressure traces at various positions on the cowl-side combustor wall for an equivalence ratio of 0.5.

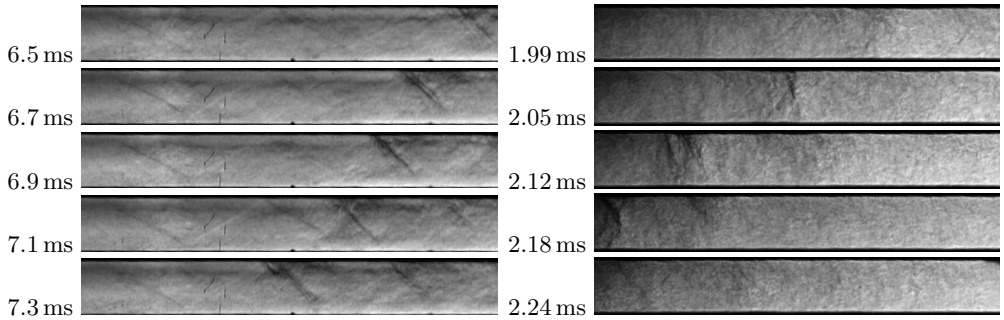

FIGURE 11. Sequence of Schlieren images showing propagation of shock-trains in the central combustion chamber: (left) (x=123-205 mm) for an equivalence ratio of 0.5; (right) (x=137-212 mm) for an equivalence ratio of 1.1.

Schlieren visualizations were captured of the propagation of this shock train in the central combustion chamber (x=123-205 mm); several of these are shown in figure 11. The appearance of the shock structures is similar to that in the corresponding images of figure 9, which, together with the qualitatively similar pressure profiles, suggests the same mechanism to be responsible. One minor difference for the lower ϕ is a shallower shock angle, indicating that weaker shocks are produced at the lower equivalence ratio. No OH* images were obtained for ϕ=0.5.

5.1.3. *ϕ=1.1*

Experiments were also carried out at higher equivalence ratios of 1.1-1.2, the intention being for the combustor to be fully choked during the steady test time. In the left part of figure 12 is shown the mean static pressure distribution on the injector-side wall from an experiment with ϕ=1.1, and this is compared with the ϕ=0.35 measurements already seen in figure 3. Instead of the steadily increasing pressure levels indicative of supersonic combustion, as obtained at the lower equivalence ratio, much higher pressure levels are now observed throughout the combustor (extending upstream of the injection point) with a generally decreasing trend downstream of injection. This is consistent with subsonic combustion conditions inside the constant-area section of the combustor. The sharp drop in pressure observed in the expansion region (x>300 mm) indicates that a sonic throat is

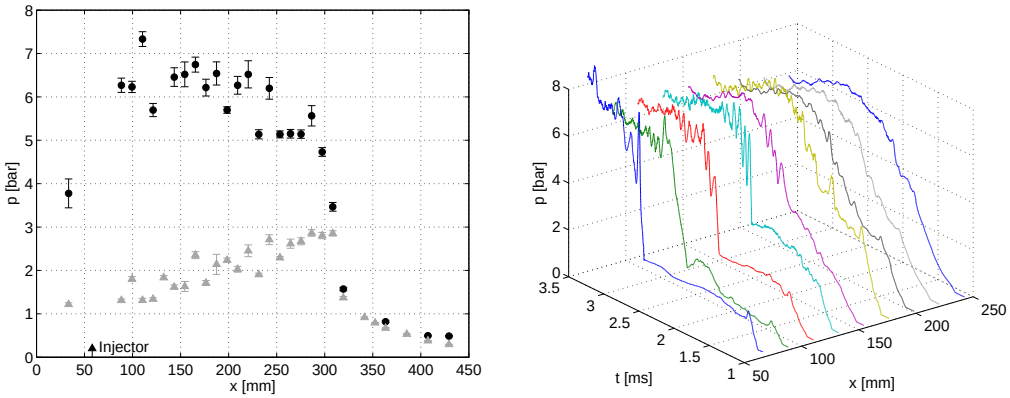

FIGURE 12. (Left) Mean pressure profiles on the injector-side combustor wall for equivalence ratios of 1.1 (○) and 0.35 (△), averaged over the steady test time. (Right) Time-resolved pressure traces at various positions on the cowl-side wall for an equivalence ratio of 1.1.

formed at the exit of the constant area section, with supersonic flow further downstream.

Although, for these high equivalence ratios, the upstream propagation of the shock train signalling the onset of choking is complete before the beginning of the steady test time, it is still instructive to compare the propagation characteristics with the other equivalence ratios studied thus far. In the right part of figure 12 are shown unsteady pressure traces on the cowl-side wall for an experiment with ϕ=1.1. The development is similar in some senses to the pictures in figures 7 and 10, but on a much-compressed time-scale. Again, oscillatory profiles are observed in the pressure traces, but these begin further upstream ($x \approx 150\,\mathrm{mm}$) than in either of the previous cases, indicating that the shock train is forming further up the combustor. Downstream of this, pressure rises without significant oscillations are observed. The quasi-periodic structures are also seen to persist further upstream than in the lower equivalence ratio cases, suggesting that the breakdown of the shock-train structure is occurring to a lesser extent here. The propagation speed of the shock train was approximately 220 m/s in these experiments.

In figure 13 is shown a sequence of quasi-synchronous Schlieren and OH* visualizations of the flow in the region immediately downstream of the injector. Propagation of the shock system up the duct is again observed, with the accompanying combustion region appearing both more intense and more strongly coupled to the leading shock in the train than at ϕ=0.7. As the system moves upstream, it appears to hesitate near the quasi-stable position seen during the ϕ=0.7 development, but then quickly moves further upstream past the injector, suggesting that the heat release is too intense for this flow topology to persist. By 3.7 ms, the entire duct is choked, with a region of intense combustion directly downstream of the injector. The lack of visible shocks in the Schlieren image suggests that the flow is now subsonic, consistent with the decreasing pressure trend in figure 12.

For these high-equivalence-ratio experiments, the most upstream pressure transducer, located 22 mm downstream of the leading edge of the injector-side wall, registered the passage of the shock train slightly before the beginning of the steady test time. However, a thermocouple located on the cowl-side wall directly opposite the injector-side leading edge did not show the passage of the shock train until after the conclusion of the test time, just prior to the onset of the unsteady oscillations discussed in § 6. These observations suggest that, during the test time, the shock system was lodged at the entrance to the combustion chamber, without fully unstarting the inlet. As the junction between the inlet

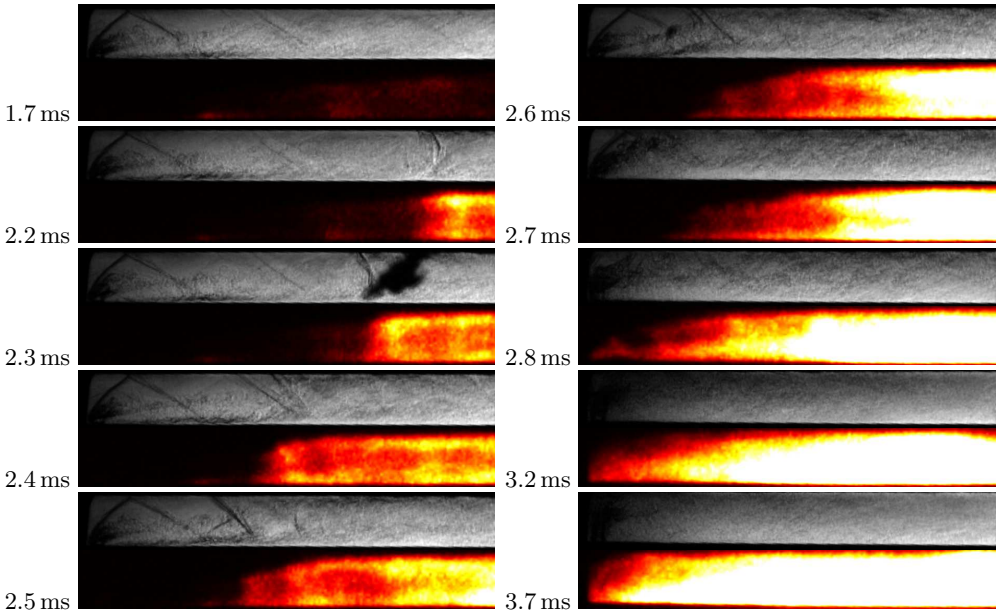

FIGURE 13. Sequence of quasi-synchronous Schlieren and OH* chemiluminescence images of the flow near the injector (x=56-136 mm) for an equivalence ratio of 1.1.

ramp and the combustor entrance is open both to the sides and through the boundary-layer bleed channel, a shock sitting at this position would allow the combustor entrance conditions to be modified without affecting the inlet flow. A configuration similar to that just described was visualized in preliminary unfuelled experiments in which insufficient drainage of the boundary-layer bleed channel had been provided. Unfortunately, in fuelled experiments, no visualizations of the combustor entrance were available to support this interpretation.

In the right part of figure 11, Schlieren images showing the onset of the shock train in the central combustion chamber for a ϕ=1.1 experiment are presented. The appearance of the nascent shock train is again similar to that in figure 9, though the leading shock in the train is now steeper. Also, the trailing shocks are less visible, which is consistent with the decreased strength of the oscillations seen in figure 12, as compared with figures 7 and 10. This may be indicative of the closer coupling between ignition and shock structure suggested by figure 13, as rapid heat release immediately behind the leading shock will drive the Mach number towards unity and decrease the strengths of the secondary shocks. The fact that such trailing shocks are still present, however, indicates that the flow downstream of the leading shock is still supersonic; the absence of the characteristic decrease in pressure associated with the ZND detonation model also suggests that conditions for a self-sustaining detonation wave have not yet been reached.

5.2. *Numerical simulations*

In order to gain further insight into the transient unstart phenomena just described and, in particular, to help isolate the responsible mechanisms, unsteady CFD simulations were performed. To minimize the computational cost, and also because of uncertainty in the exact flow conditions during the experimental start-up process, the following simplified model problem was chosen. A steady-state initial solution was first obtained for the largest stable equivalence ratio determined in § 4.2 (ϕ=0.415); the inflow pressure was

then reduced as

$$p(t) = \begin{cases} p_f - (p_f - p_0)(1 - t/t_t)^2 & \text{for } t \leqslant t_t, \\ p_f & \text{for } t > t_t, \end{cases} \tag{5.1}$$

and similarly for the inflow density, $\rho(t)$, with the inflow temperature, the inflow velocity, and the injection pressure remaining unchanged. Here, p_f was specified so as to match the computed experimental inflow pressure; the injection pressure was chosen to give the desired final equivalence ratio (after time t_t). The use of (5.1) provided a smooth transition between the initial and final equivalence ratios, and with a chosen t_t of 1 ms, was intended to roughly simulate the reduction in test-section pressure during the HEG start-up process seen in figure 1. A dual time-stepping scheme with second-order temporal accuracy and a physical time-step of 0.1 μs was applied.

5.2.1. *ϕ=0.7*

In figure 14 are shown numerical results highlighting the flow features within the combustor at different time instants during the unsteady development for a final equivalence ratio of 0.715; corresponding pressure distributions on the injector-side wall are shown in the left plot of figure 15. In the left visualization at each time-step, contours of OH mass fraction are shown in colour, with streamlines emanating from the injector indicated in black. On the lateral cut-planes, sonic lines are shown in red; boundaries of negative streamwise velocity indicating regions of separated flow are shown as red surfaces. In the visualizations to the right, pseudo-Schlieren (i.e., density-gradient magnitude) images are shown on three equally spaced planes, the first and third planes being the lateral boundaries of the computational domain. On these images are superimposed sonic lines (orange) and boundaries of flow reversal (red).

At t=0, the expected shock pattern can be observed extending down the duct. A significant subsonic region develops over a narrow region downstream of the injection port-hole, but subsonic flow is limited to the wall boundary layers throughout most of the remaining combustor domain. The OH images show that the sonic line on each lateral cut-plane lies below the main combustion region that is centred at the shear layer between the incoming air and the injected hydrogen; thus, combustion is taking place under under principally supersonic conditions at this point in time. No flow separation is visible.

At the second instant shown (t=0.65 ms), the subsonic region on the injector plane has grown considerably to encompass the entire combustor height and has also expanded laterally. The OH visualization shows that flow conditions in the main combustion region are now partially subsonic by the fourth cut-plane downstream, or more correctly, that the heat release in this region has driven the flow to subsonic conditions by this point downstream. In other words, the conditions for thermal choking have been attained locally in a stream-tube containing the main combustion region. A small incipient separation bubble is visible on the symmetry plane just downstream of injection, but separation further down the combustor is notably absent. At t=0.8 ms, the shock system near x=150 cm has strengthened significantly and begun to propagate upstream; this is also visible in the corresponding pressure trace in figure 15. At t=0.9 ms, the first appearance of separation associated with the shock train is observed on the injector-side wall. At t=1.0 ms, additional separation bubbles are visible both on the cowl-side wall and further downstream on the injector-side wall. Of further note is the embedded region of flow reversal in the middle of the combustor: this feature would explain the "two-tiered" appearance of the experimental OH* structures as the shock system approaches the injector in figure 9. The second shock in the train is now also clearly visible on the cowl-side

FIGURE 14. Numerical results of the HyShot II combustor choking process at different time instants for a final equivalence ratio of 0.715. To the left are shown contours of OH mass fraction, together with sonic lines (red), streamlines emanating from the injector (black), and boundaries of flow reversal (red surfaces). To the right are shown pseudo-Schlieren images on three equally spaced cut-planes, with sonic lines (orange) and flow reversal boundaries (red) also indicated. The axial coordinate in both cases has been compressed by a factor of two.

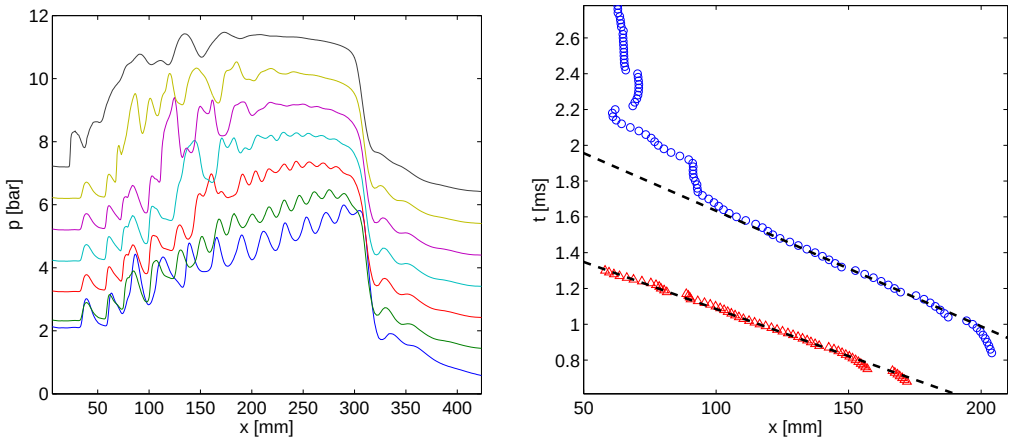

FIGURE 15. (Left) Pressure distributions on the symmetry line of the body-side combustor wall for the ϕ=0.7 numerical simulation at the time instants shown in figure 14 (lowermost, t=0.01 ms; uppermost, t=1.5 ms). All but the the first profile have been shifted upwards by an integral number of bars. (Right) Motion of the leading shock in the unsteady shock train on the cowl-side wall for equivalence ratios of ϕ=0.55 (○) and 0.72 (△); the dashed lines indicate propagation speeds of 155 and 190 m/s, respectively.

wall. Until this point, the regions of flow reversal have remained as localised separation bubbles: no large-scale separation behaviour is evident.

In contrast to the corresponding experiments, no significant pausing of the shock-train motion is observed near the injection location; rather, just a slight hesitation occurs around the time of the second-to-last instant shown (t=1.2 ms) as the leading shock interacts with the injection jet to modify the flow topology near the injector. The shock motion then continues upstream (t=1.5 ms), but now as a two-dimensional shock train associated with a large-scale separation region on the injector-side wall. An embedded supersonic core remains, extending down the entire length of the combustor. The corresponding pressure profile in figure 15 shows a pressure rise beginning upstream of the injector, followed by an extended plateau region. The instantaneous behaviour here is thus similar to a dual-mode scramjet with an oblique shock train located in the isolator.

In the right part of figure 15 is plotted the motion of the leading shock on the cowl-side wall in the form of an x-t diagram (the result from a computation with another equivalence ratio, to be discussed shortly, is also shown). The shock positions were estimated by setting an appropriate pressure threshold and, at each time step, calculating the first downstream point at which this threshold was exceeded. The formation point of the incipient shock train is somewhat upstream of the corresponding point in experiments: a location of approximately 170 mm was determined from the numerical pressure traces and Schlieren images, whereas the first appearance of the shock train in experimental Schlieren images occurs at approximately 200 mm. The numerical shock accelerates as it forms but soon reaches a roughly constant speed; the plotted line shows this to be approximately 190 m/s, significantly higher than in the corresponding experiments. Small hesitations are observed as the shock train approaches the injector, but the significant slowing seen in figure 8 is not observed. As a result of both the absence of pausing and the higher overall propagation speed, the shock train has reached the injection location within ∼0.6 ms of its formation, much more quickly than in experiments. Possible explanations for these discrepancies between experimental and numerical behaviours are discussed in § 8.

5.2.2. *ϕ=0.55*

To examine the effects of varying the equivalence ratio on the unsteady behaviour in the numerical model, a further simulation with a final value of ϕ=0.553 was performed. The initial behaviour in this case is similar to that at the higher equivalence ratio. The transient development again appears to be triggered by the sonic line crossing the main combustion region towards the rear of the combustor. A shock train begins forming within 0.2 ms and commences propagating up the duct; in this case, separation bubbles appear almost immediately on the injector-side wall and accompany the shock train upstream. However, the extent of the separation regions again remain limited during propagation and, while they may promote the choking development by providing an effective area contraction, it is evident that they are not the primary driving mechanism. As the leading shock approaches the injection location, its motion begins to falter, and it undergoes several "hesitations" before merging with the injector barrel-shock. At this point, the flow finds a quasi-stable configuration with no further propagation of the shock train; this behaviour is similar in nature to that observed in the ϕ=0.7 experiments, but the flow topologies differ in the two cases.

The motion of the leading shock on the cowl-side wall is plotted in the right part of figure 15. Comparing to the higher equivalence ratio, the shock train now originates further back in the combustor (from ≈200 mm) and propagates upstream at a slower speed: the dashed line indicates a value of 155 m/s. A deceleration of the shock system is seen from approximately 120 mm, similar to the experimental behaviour for ϕ=0.7 (in ϕ=0.5 experiments, the test period had already concluded by the time the shock train had reached a comparable point upstream); this is followed by the termination of the upstream motion when the shock system merges with the injection shock. A large discrepancy is again obtained between the experimental and numerical propagation speeds: the numerical value for ϕ=0.5 is significantly higher even than the experimental ϕ=0.7 value.

6. Inlet unstart

As stated in § 5.1.1, the effective equivalence ratio increases monotonically after the conclusion of the test time due to the falling reservoir pressure. For clarity, in this section we thus refer to the steady equivalence ratio (i.e., the average value during the test time that has simply been denoted ϕ until now) as ϕ_s, with ϕ_u referring to the time-varying quantity. At some point after the test time in all combustion experiments, large-scale pressure oscillations were observed to develop inside the combustion chamber. The point in time at which these oscillations first appeared depended on the steady equivalence ratio: for ϕ_s=1.1 experiments, the onset occurred as early as 8 ms after shock reflection, whereas for lower steady equivalence ratios it was somewhat later. In § 2.1, we concluded that the flow has not yet been significantly contaminated by driver gas at 12 ms; thus, it is possible to draw conclusions about the combusting flow up to at least this point in time. The left part of figure 16 shows one example of the observed oscillatory behaviour: here, the unsteady equivalence ratio is plotted together with time-resolved pressure traces at several positions on the injector-side wall for an experiment with ϕ_s=1.1. The oscillations from roughly 8 ms are similar to those documented, for example, by Tan & Guo (2007) and Wagner *et al.* (2009) for an unstarted inlet (this oscillatory behaviour is often referred to as "buzzing" and is caused by periodic gorging and disgorging of the inlet shock system). At the onset of the oscillations, the unsteady equivalence ratio has risen to approximately 1.3; for ϕ_s=1.1, onset values between 1.3 and 1.4 were found to be typical.

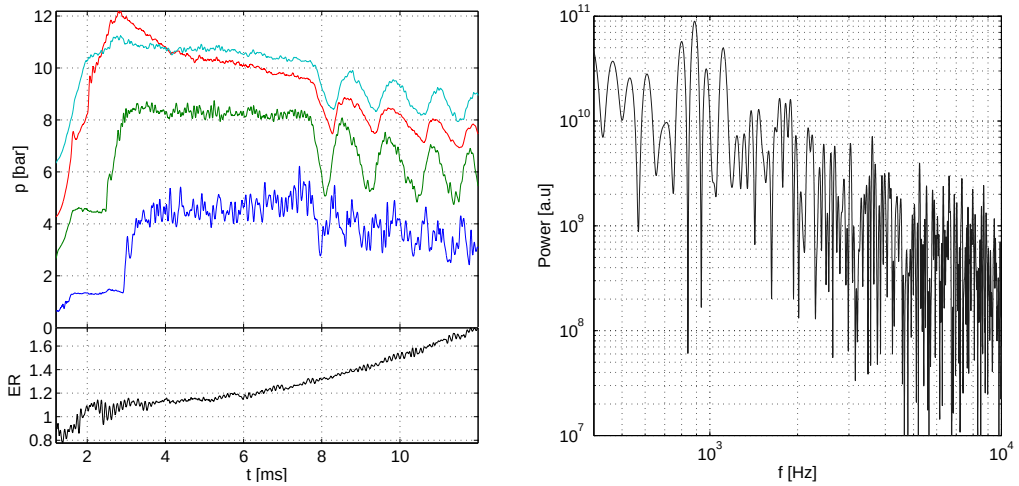

FIGURE 16. (Left) Time-resolved pressure development inside the combustor compared to the time development of the equivalence ratio. The pressure traces are on the injector-side wall at x locations of 33 (lowermost), 88, 187, and 297 mm (uppermost); all but the first trace have been vertically shifted for clarity. (Right) Power spectrum of the pressure trace at 88 mm during the "buzzing" phase.

In ϕ_s=0.7 experiments, the first appearance of buzzing was later, typically between 11 and 12 ms, and at lower unsteady equivalence ratios of between 1.05 and 1.1. The onset of "buzzing" is thus not determined solely by the instantaneous value of ϕ_u. In figure 16, the oscillations are clearly visible in the traces from transducers downstream of the injection location (58 mm); they are less clear in the trace from upstream of the injection point, but the power spectrum of this signal showed similar peaks to those of the downstream traces, if slightly weaker. Also apparent in the oscillatory profiles is a phase-shift between measurement locations due to the lag from the pressure signal travelling down the duct.

In the right part of figure 16 is shown the power spectrum from the transducer located at 88 mm; this spectrum is typical of the transducers downstream of the injection point. Because of the steady decrease in the pressure, there is significant energy in the low-frequency part of the spectrum, but we also observe a strong group of peaks centered at approximately 900 Hz; weaker harmonics can be discerned near 1800 and perhaps 3600 Hz. Assuming the oscillations to be acoustic in nature, we may estimate the resonant modes, following Newsome (1984), by considering waves (compression or expansion) travelling at speeds $\overline{a}+\overline{u}$ and $\overline{a}-\overline{u}$, respectively, up and down the combustor: here $\overline{a}$ is the mean sound speed and $\overline{u}$ is the mean flow velocity, each averaged in an appropriate manner. The frequencies of the fundamental and higher modes for a duct of length L that is open at both ends are then

$$f_n = \frac{n\overline{a}}{2L}(1-\overline{M})(1+\overline{M}), \quad n = 1, 2, 3, \ldots \tag{6.1}$$

where $\overline{M} = \overline{u}/\overline{a}$. For the present model, the length of the duct (from the cowl leading edge to the end of the constant-area section) is 367 mm. The speed of the pressure disturbance propagating in the downstream direction, $\overline{a}+\overline{u} = \overline{a}(1+\overline{M})$, can be estimated by correlating the oscillatory pressure signal between the different measurement locations. The speed thus determined was found to increase down the duct, as would be expected for heat addition in a constant-area subsonic flow, with a mean value between 88 and 297 mm of approximately 1600 m/s. This likely overestimates the overall mean speed

(including the section ahead of the injector) slightly, so we assume a representative value of 1500 m/s. It thus remains to estimate $1-\overline{M}$, which we do as follows. We have already noted that the core flow (i.e., outside the wall boundary layers) is sonic at the exit of the constant-area section. The conditions at the combustor entrance depend on the intake shock structures, which are here imposed by the downstream subsonic flow, but the entrance Mach number is relatively insensitive to the exact nature of these shock structures. For example, a single strong shock at the inlet (with a deflection angle of 3.6°) gives a post-shock Mach number of 0.40, whereas a weak shock with a turning angle of 21.6° (i.e., the ramp angle) followed by a strong shock gives a value of 0.49. Since unstart is characterized by a displacement of the original shock system out of the inlet, the former value is probably more appropriate. Thus, assuming M=0.4 until the injector, rising to M=1 at the exit, a mean value of $\overline{M}$=0.6 seems reasonable and is probably accurate to within 0.1. Substituting these estimated values into (6.1) gives f_1=820 Hz, which, considering the approximations made in the analysis, agrees well with the observed band of frequencies.

7. Discussion of experimental and computational results

As noted in § 5.1, Frost *et al.* (2009) interpreted the unsteady choking phenomena in the HyShot II combustor at equivalence ratios slightly above 0.5 to be associated with boundary-layer separation. Based on this assumption, they used their results to test the validity of the boundary-layer-separation criterion due to Korkegi (1975). This criterion was developed for shock-induced boundary-layer separation, but Frost *et al.* concluded from their measurements that it is also appropriate for the more gradual pressure increases encountered in supersonic combusting flows. Thermal choking was ruled out as a mechanism for the choking behaviour based on a simple Rayleigh-type flow analysis. A similar analysis in § 4.2 of the present work also led to the conclusion that the onset of boundary-layer separation should precede that of thermal choking.

However, in both the experiments and the unsteady numerical simulation at ϕ=0.7 in the present work, we have seen that the transient flow and combustion phenomena that develop within the combustion chamber at the onset of choking are consistent with thermal choking, rather than boundary-layer separation, as the responsible mechanism. While the experimental results were less extensive at ϕ=0.5, and the findings thus less conclusive, the results obtained suggested the same mechanism to be responsible as in the higher-ϕ case; this was confirmed by the corresponding numerical simulation. The immediate implication is that, although boundary-layer separation may have occurred at some point during the choking development in the experiments of Frost *et al.* (2009), their assumption that it was the driving mechanism is likely in error. The conclusion of these authors regarding the validity of the Korkegi criterion is therefore also questionable, especially considering their use of the peak pressure during the steady test period as the incipient separation pressure, since there is no reason to believe that these two values should coincide.

A more important conclusion from the present results regards the nature of thermal choking in scramjet engines and the apparent inability of a simple Rayleigh-type analysis of the heat release within the combustion chamber to provide an adequate quantitative prediction for the onset of thermal choking. We attribute this to the one-dimensional approximation of the Rayleigh analysis, whereby the flow conditions are assumed to be uniform across the duct. The numerical simulations here have shown that, contrary to this assumption, the combustion-related heat release occurs principally over a relatively limited cross-sectional area of the flow, centered around the shear layer between the in-

coming air free-stream and the injected hydrogen. Thus, the reduction in Mach number over the stream-tube that covers this main combustion region may be significantly larger than that which would result from uniform heat release across the duct, thus leading to an earlier onset of thermal choking. If such "local" thermal choking occurs, however, the possibility remains for the flow to adjust itself through the generation of upstream-propagating disturbances, resulting in a modified flow configuration in which the heat release is redistributed away from the choked stream-tube(s). Thus, new steady or quasi-steady flow topologies may arise in constant-area ducts, without the full inlet unstart that will almost always result from the global thermal choking limit being reached (new topologies may be possible in the latter case if, for example, the overall combustion efficiency is reduced or the injector flow is affected: these possibilities cannot be completely ruled out, but appear unlikely to occur in practice). Such quasi-steady topologies were observed in the present work, in both ϕ=0.7 experiments and the ϕ=0.5 computation.

That the localized nature of the heat release in scramjet engines could lead to a significant drop in the local Mach number was recognised as early as Ferri (1968); however, he saw no problem with the flow passing smoothly from supersonic to subsonic conditions and suggested it would lead to an embedded region of reversed flow, rather than the unsteady choking behaviour observed here. The possibility of such a deceleration in one-dimensional flows, given the right combination of changes in area, stagnation temperature and frictional length, was also noted by Shapiro (1953). He writes, however (pp. 236), "the continuous transition from supersonic to subsonic speeds, ..., is hardly ever realized in practice, and is probably unstable under most conditions."

In discussing figures 7 and 10, it was noted that the well-defined periodic structures in the time-resolved pressure traces, indicating the passage of the shock train, appeared to break down from $x\approx$150 mm, suggesting a disruption in the regular shock structures during the upstream propagation. A likely explanation for this is the onset of boundary-layer separation on the injector-side wall. In discussing the upstream visualizations of figure 9, we noted that the unsteady structures associated with the presumed separated flow region had a strongly disrupting effect on the flow downstream of the leading shock. Linking the breakdown of the shock train to the onset of flow separation is also consistent with the approximate positions at which the two phenomena were determined to occur. Disruptions in the trailing shock structures as the shock train propagated upstream were also observed in the numerical simulations; however, the much quicker propagation in comparison to the experiments made it difficult to draw definite conclusions as to whether these disruptions were linked to the development of the separated flow regions.

8. Simplified theoretical analysis

8.1. *Quasi-unsteady Rayleigh flow model*

In order to gain a better understanding of the transient processes observed in the experiments and computations described thus far, a simple one-dimensional quasi-unsteady analysis was performed. While it was concluded in the previous section that such one-dimensional analyses fail to predict adequately, for example, the onset of thermal choking in complex three-dimensional flows, they can nevertheless provide valuable insights into the qualitative nature of the phenomena encountered. The present analysis is based on a conventional steady Rayleigh-flow problem, i.e., stagnation temperature change through heat addition in a constant-area duct, but includes a moving normal shock within the flow domain. It is a well-known property of Rayleigh flow that, whether the initial Mach number is subsonic or supersonic, heat addition drives the flow towards sonic condi-

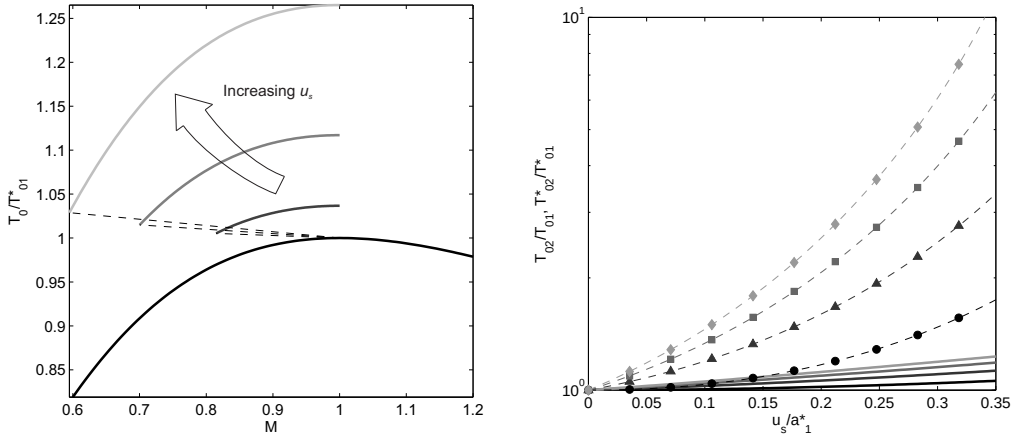

FIGURE 17. (Left) Curves of stagnation temperature versus Mach number assuming conventional Rayleigh flow (base curve) and Rayleigh flow following an upstream-propagating normal shock of speed u_s, inserted at the original Rayleigh-flow choking point. (Right) Stagnation temperature ratios, T_{02}/T_{01} (solid lines), and choking stagnation temperature ratios, T^*_{02}/T^*_{01} (dashed lines/symbols), through an upstream-propagating normal shock with normalised speed u_s/a^*_1 (the T^*_{02}/T^*_{01} curves assume choking through Rayleigh flow on either side of the shock). The four curves in each case are for pre-shock Mach numbers of ($\circ$-darkest) 1.0, ($\triangle$) 1.5, ($\square$) 2.0 and ($\diamond$-lightest) 2.5.

tions, and once this sonic state is reached, no further heat addition is possible without a modification to the inflow conditions. It is precisely such excess heat addition that was determined to give rise to the choking behaviour in the present study.

If a stationary normal shock is introduced into the flow, it does not alter the situation just described, as the stagnation temperature is constant through such a shock. However, the picture changes if the shock position is unsteady. This is because, in a frame-of-reference in which the shock is moving, neither the stagnation temperature nor the choking stagnation temperature (assuming conventional Rayleigh flow otherwise) is constant across the shock. This is demonstrated in figure 17. In the left plot, curves of the stagnation temperature, T_0 (normalised by the pre-shock choking stagnation temperature, T^*_{01}), are plotted against the flow Mach number, M, for constant-area frictionless flow. The base curve (darkest) shows the standard Rayleigh relation, with T_0/T^*_{01}=1 at M=1. A steady normal shock inserted at any point on the supersonic branch of this curve will simply shift the flow state horizontally to the subsonic branch, without any change to either T_0 or the choking stagnation temperature, T^*_0. If the shock is moving, however, the post-shock state will no longer lie on this curve. To see this, we introduce shocks with various upstream propagation speeds, u_s, at the Rayleigh choking point, M=1 (we make this particular choice since it is the incipient shock formation point). The pre- and post-shock states for three shocks of increasing strength are joined by dashed lines on figure 17; for each of these, the subsonic branch of the Rayleigh curve starting from the post-shock state is also shown. As may be seen, there is a small stagnation temperature rise through each moving shock, but much more significant is the rise in choking stagnation temperature, i.e., T_0/T^*_{01} at M=1. In effect, the propagating shock gives the flow more "room" for heat to be subsequently added before choking occurs. This is due to the larger drop in Mach number in comparison to a stationary shock, contributed to by both a larger velocity decrease and a greater increase in the sound speed across the shock.

This effect is demonstrated quantitatively in the right plot of figure 17. Here, both the stagnation temperature ratio, T_{02}/T_{01} (solid lines), and the choking stagnation temper-

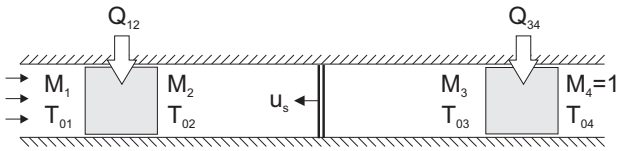

FIGURE 18. Simplified model of heat release and quasi-unsteady shock propagation in a constant-area combustion chamber.

ature ratio, T_{02}^*/T_{01}^* (dashed lines/symbols), across the shock are plotted as functions of the normalised shock speed in the laboratory frame, u_s/a_1^*, where a_1^* is the Rayleigh-flow choking sound speed at pre-shock conditions. The subscripts 1 and 2 refer here to pre- and post-shock conditions, respectively. Results for pre-shock Mach numbers of M_1=1, 1.5, 2 and 2.5 are shown; a ratio of specific heats of γ=1.4 is assumed in all cases. Monotonic increases in T_{02}/T_{01} and T_{02}^*/T_{01}^* with both u_s/a_1^* and M_1 are observed. Both T_{02}/T_{01} and T_{02}^*/T_{01}^* are always greater than unity for $u_s > 0$ (i.e, upstream shock propagation), but the rise in stagnation temperature is negligible in comparison to that in the choking stagnation temperature. In fact, the moving shock provides a mechanism that would potentially allow infinite energy to be added to the flow before choking occurs, since $T_{02}^*/T_{01}^* \to \infty$ as we tend to the limit of a zero post-shock flow velocity (in the laboratory frame-of-reference).

8.2. *Application of quasi-unsteady model to scramjet combustor*

To determine the implications of this behaviour for the supersonic combustion configuration under investigation in the present work, we construct a simplified one-dimensional model as shown in figure 18. Two regions of conventional Rayleigh flow, with total heat additions of Q_{12} and Q_{34}, respectively, are separated by a normal shock moving up the duct at a constant speed, u_s (the use of the term "quasi-unsteady" to describe the model refers to the stipulation that u_s is constant). The flow is assumed to be thermally choked after the second region of Rayleigh flow (i.e., $M_4 = 1$): it is precisely this choking that drives the shock motion upstream. This assumption is similar in some senses to the Chapman-Jouget (C-J) condition for a detonation wave, except the sonic condition is applied in the laboratory frame rather than in one moving with the shock. In general, this will result in a lower shock-propagation speed than the C-J condition, since M_3 will be smaller than the post-shock Mach number in the shock frame by an amount u_s/a_3; thus, a larger Q_{34} will be required to reach sonic conditions.

There are several significant approximations inherent to this model. First, frictional and mass-addition effects are ignored, as are any changes to the physical properties of the gases due to combustion. Furthermore, for the shock speed to be constant, we must assume that Q_{12} and Q_{34} have been unchanging for sufficient time that the downstream choking location has been able to communicate with the shock and establish a quasi-unsteady configuration; thus, either the shock propagation speed must be small or the heat-addition regions must be physically separated from the shock. More formally, a condition such as $u_s(dQ/dx)/Q_{tot} \ll \overline{a}/(2d)$ can be specified, where $Q_{tot} = Q_{12} + Q_{34}$, d is the distance between the shock and the choking location, $\overline{a}$ is the mean sound speed in this region, and dQ/dx is evaluated at the shock location. This assumption will become increasingly approximate as the shock approaches the injection location, as the streamwise derivative of the heat release is typically greatest there (Curran *et al.* 1996). A true unsteady calculation with time-dependent Q_{12} and Q_{34} may be possible, but this would significantly complicate the analysis. It is further assumed that the coupling between the shock propagation and the downstream heat release region is in the laboratory frame; an

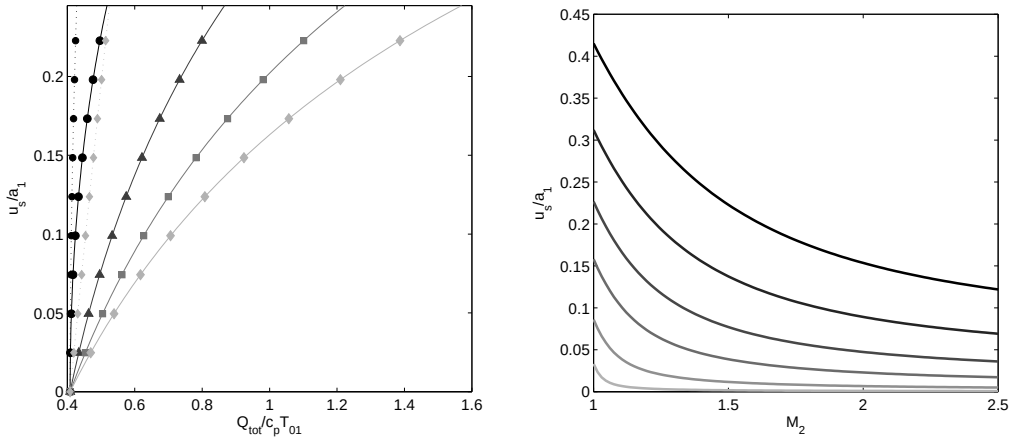

FIGURE 19. (Left) Curves of the normalized shock speed, u_s/a_1, versus the normalised total heat release for the simplified unsteady-Rayleigh model shown in figure 18, assuming M_1=2.5, and for pre-shock Mach numbers of M_2=($\circ$) 1.0, ($\triangle$) 1.5, ($\square$) 2.0 and ($\diamond$) 2.5. The dotted curves show the equivalent Chapman-Jouget detonation wave speeds for M_2=1.0 and 2.5. (Right) Curves of u_s/a_1 versus M_2 for (light to dark) Q_{tot}/c_pT_{01}=0.41, 0.42, 0.45, 0.5, 0.6 and 0.8.

example where this is not the case is a detonation wave, where the coupling is in the shock frame. Finally, we assume a single normal shock, rather than the shock train observed in experiments and computations. Considering a control volume around a shock train and assuming both that viscous losses are negligible and that conditions are uniform across the inlet and exit planes of the control volume, the resulting conservation equations are exactly the same as for a single normal shock (Heiser & Pratt 1994), and thus so are the post-shock properties. However, for an extended shock train, the earlier assumption that the "shock" is physically separated from the heat-addition regions becomes less tenable. In light of these points (as well as the considerable approximation inherent in the one-dimensional assumption), we cannot expect this model to make accurate quantitative predictions of the shock speed under realistic combustion conditions; rather, we employ it here to provide insight into the qualitative behaviour of the choking shock motion.

In order to be consistent with the entrance conditions of the HyShot II combustion chamber in the present investigation, we assume an initial Mach number, M_1, of 2.5. The shock speed is then uniquely determined by the chosen values of Q_{12}/c_pT_{01} and Q_{34}/c_pT_{01}, through the Rayleigh-flow and normal-shock relations. In the left plot of figure 19 is shown the normalised shock speed, u_s/a_1, as a function of the total heat addition, $Q_{tot}/c_pT_{01} = (Q_{12} + Q_{34})/c_pT_{01}$, for different distributions of Q_{tot} between Q_{12} and Q_{34}: four curves for choices of Q_{12} such that M_2=1.0, 1.5, 2.0 and 2.5 are plotted. The value of M_2 can be roughly correlated to the position of the shock within the combustor: M_2=1 corresponds to the location at which the incipient shock forms and M_2=M_1=2.5 to shock propagation upstream of injection. First, we note that for this choice of M_1, the minimum heat addition for choking, and thus the formation of an unsteady shock, is Q_{tot}/c_pT_{01}=0.409. From this value, the shock speed rises monotonically with increasing total energy addition for all M_2. For M_2=1, the shock speed rises extremely rapidly with Q_{tot}, the slope of the curve being infinite at the incipient shock formation point. Thus, the initial shock speed is very sensitive to the total heat addition, which may explain to some extent the disagreement between the experimental and computational shock speeds in § 5. The normalised experimental shock speed for ϕ=0.7, for

example, is u_s/a_1=0.13, which corresponds to Q_{tot}/c_pT_{01}=0.44 for M_2=1; this compares to u_s/a_1=0.26 and Q_{tot}/c_pT_{01}=0.53 for the numerical result.

A second observation is that, for a given Q_{tot}/c_pT_{01}, the shock speed slows as the Mach number ahead of the shock, M_2, increases. This is shown more clearly in the right plot of figure 19, in which u_s/a_1 is plotted against M_2 for several values of Q_{tot}/c_pT_{01} between 0.41 and 0.8. Thus, we would expect a decrease in the propagation speed as the shock propagates up the duct. This is consistent with the observed experimental behaviour in figure 8, and also the numerical result for ϕ=0.5 shown in figure 15. That no notable slowing was observed in the ϕ=0.7 simulation is probably due to the accelerated time-scale of the flow development, meaning that the choking location at the combustor exit did not have sufficient time to communicate with the moving shock and retard its progress as it moved upstream.

Also shown in the left plot of figure 19 are corresponding curves for the C-J detonation wave-speeds with M_2=1.0 and 2.5; here, Q_{34} is equated with the enthalpy change across the detonation wave. As predicted earlier, the detonation wave speeds are significantly higher than the equivalent choking shock speeds. Again, an extremely rapid increase of u_s/a_1 with Q_{tot}/c_pT_{01} - even more so than in the corresponding choking shock curve - is observed for M_2=1.0.

Employing different values of the initial Mach number, M_1, results in similar curves to those seen in figure 19. A higher M_1 shifts the choking limit of Q_{tot}/c_pT_{01} to a larger value, but the qualitative trends remained identical.

8.3. *Comparison of thermal and area-contraction choking*

As noted in § 1, a common practice to reproduce scramjet-like choking behaviour in non-combusting flows is to employ mechanical throttling, i.e., to introduce a flow obstruction to simulate the combustion-induced pressure rise. If the resulting area reduction is sufficient to introduce a physically choked throat, such throttling could conceivably be employed to simulate unsteady thermal choking processes such as those observed in the present work. The simplified model developed in this section provides a convenient means to compare the unsteady behaviour in the two cases (physical and thermal choking), and in particular, to estimate the range of heat-release conditions that mechanical throttling can reproduce (based on the criterion of equal shock speeds). For physical choking, we assume a situation similar to that shown in figure 18, but with the first heat-release region (Q_{12}) removed and the second (Q_{34}) replaced by an isentropic compression with a minimum area ratio A^*/A at x^*. For a given M_1, and assuming the back-pressure is sufficiently low that a sonic throat forms at x^*, the shock speed is uniquely determined by the value of A^*/A. To match this shock speed with that produced by thermal choking, we must choose particular values of Q_{12}/Q_{tot}, or alternatively M_2. Two values of special interest are M_2=1, corresponding to the onset of the unsteady choking behaviour, and M_2=M_1 (i.e., Q_{12}=0). This latter choice corresponds to the propagation of the shock (system) in the isolator ahead of the injection point, which is the phase of the unsteady flow development that mechanical throttling is most suitable for simulating.

Before proceeding to discuss the relevant results, a key difference between physical and thermal choking in this context should be noted. The total heat release necessary to induce thermal choking is not affected by the introduction of a stationary normal shock, as the stagnation temperature does not change across such a shock. In contrast, except for the trivial case of initially sonic flow, the isentropic area-contraction ratio necessary to induce physical choking is altered if a stationary shock is inserted in the flow. The critical area ratio for the onset of choking from post-shock (i.e., subsonic) conditions, $(A^*/A)_{sub}$, is invariably larger than that from pre-shock (supersonic) conditions,

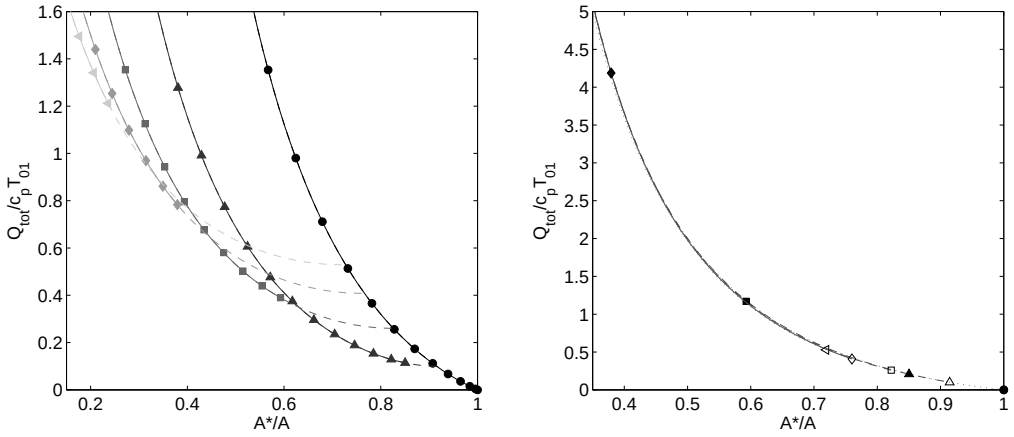

FIGURE 20. A comparison of the thermal and area-contraction choking characteristics required to produce equivalent quasi-unsteady flows. The total heat addition is plotted against the choking area ratio producing the same shock propagation speed, assuming (left) M_2=1 and (right) $M_2 = M_1$ in the thermal choking model. The initial Mach numbers are M_1=(○, $\cdots\circ\cdots$) 1.0, (△, $-\cdot-\triangle-\cdot-$) 1.5, (□, $---\square---$) 2.0, (◇, —◇—) 2.5 and (◁, $\cdots\triangleleft\cdots$) 3.0. In the left plot, the dashed part of the curve indicates area ratios between $(A^*/A)_{sub}$ and $(A^*/A)_{super}$; in the right plot, these two points for each curve are indicated by open and closed symbols, respectively.

$(A^*/A)_{super}$. Thus, if we imagine starting with a configuration in which $A^*/A = 1$ and then steadily decreasing A^*/A (while keeping the compression isentropic), the flow will remain shock-free until $(A^*/A)_{super}$ is reached, at which point a shock will form and immediately begin to propagate upstream with a non-zero velocity. If A^*/A is subsequently increased during the shock propagation, expansion waves will travel upstream and reduce the propagation speed until the shock becomes stationary at $(A^*/A)_{sub}$. Further increases in A^* will unchoke the duct. Thus, in this idealized case of isentropic area-contraction choking, a hysteresis in the shock propagation behaviour will be observed; a similar effect is used in the starting of variable-geometry supersonic inlets (Shapiro 1953). No such behaviour will be exhibited for thermal choking. In reality, however, the supersonic contraction is unlikely to be isentropic, and the formation of oblique shocks, with resulting shock/boundary-layer interactions, will promote the onset of boundary-layer separation, which may itself trigger the choking development before $(A^*/A)_{super}$ is reached.

Returning now to specific results, in the left plot of figure 20 are curves showing the area ratios required to reproduce the same shock speed as heat releases of Q_{tot}/c_pT_{01}, assuming M_2=1 (i.e., the shock formation point for thermal choking), for five initial Mach numbers between 1 and 3. In light of the discussion in the previous paragraph, all but the M=1 curve is divided into two parts: the left branches (solid-symbols) correspond to area ratios below $(A^*/A)_{super}$, whereas the right branches (dashed) cover area ratios between $(A^*/A)_{super}$ and $(A^*/A)_{sub}$. The left branch of each curve thus represents conditions that are achievable through a one-way isentropic reduction in A^*/A. As the initial Mach number is increased, the minimum value of Q_{tot}/c_pT_{01} for choking becomes larger, and both $(A^*/A)_{super}$ and $(A^*/A)_{sub}$ show corresponding reductions. $(A^*/A)_{super}$ is affected more strongly, which leads to a growing discrepancy between the values of Q_{tot}/c_pT_{01} at the two choking area ratios. For M_1=2.5, for example, the heat release corresponding to $(A^*/A)_{super}$, $Q_{tot}/c_pT_{01} \approx 0.75$, is almost double that at $(A^*/A)_{sub}$. Referring to the M_2=1 curve in figure 19, we see that heat release values of this magnitude would produce shock speeds well in excess of those observed in practice (for example, the experimentally observed value of u_s/a_1 for ϕ=0.7 was approximately 0.13). These results suggest that it

becomes increasingly difficult for area-contraction choking to reproduce relevant thermal choking behaviour as the initial Mach number is increased much above unity.

Similar curves are shown in the right part of figure 20 for M_2=M_1, representing the shock propagation behaviour upstream of injection. In this case, the curves for the different initial Mach numbers lie very close to one another; thus, for clarity, $(A^*/A)_{sub}$ and $(A^*/A)_{super}$ for each Mach number are plotted using open and closed versions, respectively, of the same symbol. Similar comments apply here as in the left plot of figure 20, but we note the significantly larger values of Q_{tot}/c_pT_{01} corresponding to $(A^*/A)_{super}$. This is especially the case for the higher Mach numbers considered: for M_1=3.0, the relevant point lies well off the plotted scale. Thus, even for studying transient choking phenomena in isolators, mechanical throttling appears limited to shock propagation behaviours dominated by flow separation. This conclusion is consistent with the experimental findings of Wagner *et al.* (2009), for example.

9. Conclusions

A series of experiments has been carried out in the HEG shock-tunnel facility to investigate the transient fluid-combustion phenomena that develop in the HyShot II combustor under high-equivalence-ratio conditions. In addition to surface pressure measurements on the injector- and cowl-side walls, high-speed flow visualization in the form of pulsed-diode laser Schlieren and OH* chemiluminescence was employed. Schlieren images revealed that the unstart process begins with the development of a shock train in the central-to-rear combustion chamber that subsequently propagates upstream. Although both the location of the onset of this shock train and its speed of propagation were found to depend strongly on the equivalence ratio, the physical nature of the system appeared similar in all cases. OH* visualizations did not indicate the presence of strong separation features propagating upstream with the shock train near its point of formation, suggesting that the driving mechanism for the transient development was thermal choking. However, boundary-layer separation was observed to develop on the injector-side wall when the shock train had moved further upstream, and the resulting unsteady flow features were seen to interact strongly with the shock-train structure.

Unsteady numerical simulations of the experimental configuration were performed using the DLR TAU code. These confirmed the main qualitative findings from the experiments, but revealed that, at ϕ=0.55, localised boundary-layer separation accompanied the onset of thermal choking in the combustor, whereas at ϕ=0.72, separation did not develop until later in the shock-train propagation. Significant discrepancies were observed between the experimental and computational shock-propagation velocities at nominally equal equivalence ratios. The computations also indicated that the global choking behaviour was dictated by the limited region of maximum heat release at the shear layer between the incoming air stream and the injected hydrogen. This led to the concept of "local" thermal choking and suggested that integral estimates based on one-dimensional assumptions give unreliable quantitative predictions regarding the onset of thermal choking. Further, such localised choking behaviour can result in the development of new quasi-steady flow topologies, which were observed in both ϕ=0.7 experiments and the ϕ=0.55 numerical simulation.

Following full inlet unstart in the experiments, high-amplitude pressure oscillations were observed to develop in the combustion chamber; the frequency content of the measured signals was found to be consistent with a simple acoustic analysis.

A one-dimensional quasi-unsteady model based on Rayleigh flow was proposed to explain aspects of the transient behaviour. In particular, this model predicts a slowing of

the shock train as it moves upstream, a phenomenon that was observed experimentally. It also predicts the initial shock propagation speed to be very sensitive to the total heat release, which may explain the observed discrepancies between experimental and numerical shock speeds. Finally, by constructing an equivalent model for area-contraction-based choking, the difficulty of employing mechanical throttling to reproduce relevant thermal choking behaviour in scramjet combustion chambers and isolators was highlighted.

This work was performed within the "Long-Term Advanced Propulsion Concepts and Technologies II" (LAPCAT II) project investigating high-speed transportation. LAPCAT II, coordinated by ESA-ESTEC under the supervision of Johan Steelant, is supported by the EU within the 7th Framework Program, Theme 7 TRANSPORT, Contract no.: ACP7-GA-2008-21 1485. The authors wish to acknowledge the assistance of the HEG technical staff, in particular Ingo Schwendtke and Mario Jünemann, in preparing the experiments, and Moritz Schmidt in the design of the model.

REFERENCES

Bertin, J.J., Stetson, K.F., Bouslog, S.A. & Caram, J.M. 1997 Effect of isolated roughness elements on boundary-layer transition for Shuttle Orbiter. *J. Spacecraft Rockets* **34** (4), 426–436.

Boyce, R.R., Paull, A., Stalker, R.J., Wendt, M., Chinzei, N. & Miyajima, H. 2000 Comparison of supersonic combustion between impulse and vitiation-heated facilities. *J. Prop. Power* **16** (4), 709–717.

Curran, E.T., Heiser, W.H. & Pratt, D.T. 1996 Fluid phenomena in scramjet combustion systems. *Annu. Rev. Fluid Mech.* **28**, 323–360.

Do, H., Im, S., Mungal, M.G. & Cappelli, M.A. 2011 The influence of boundary layers on supersonic inlet flow unstart induced by mass injection. *Exp. Fluids* **51** (3), 679–691.

Ferri, A. 1968 Review of SCRAMJET propulsion technology. *J. Aircraft* **5** (1), 3–10.

Frost, M.A., Gangurde, D.Y., Paull, A. & Mee, D.J. 2009 Boundary-layer separation due to combustion-induced pressure rise in supersonic flow. *AIAA J.* **47** (4), 1050–1053.

Gardner, A.D., Hannemann, K., Steelant, J. & Paull, A. 2004 Ground testing of the Hyshot supersonic combustion flight experiment in HEG and comparison with flight data. AIAA Paper No. 2004-3345, July 2004.

Gerhold, T., Friedrich, O., Evans, J. & Galle, M. 1997 Calculation of complex three-dimensional configurations employing the DLR TAU-code. AIAA Paper No. 97-0167, 1997.

Gerlinger, P. 2001 An implicit multigrid method for turbulent combustion. *J. Comput. Phys.* **167**, 247–276.

Haber, L.C. & Vandsburger, U. 2003 A global reaction model for OH* chemiluminescence applied to a laminar flat-flame burner. *Comb. Science Tech.* **175**, 1859–1891.

Hannemann, K. 2003 High enthalpy flows in the HEG shock tunnel: Experiment and numerical rebuilding. AIAA Paper No. 2003-978, Jan. 2003.

Hannemann, K., Karl, S., Schramm, J. Martinez & Steelant, J. 2010 Methodology of a combined ground based testing and numerical modelling analysis of supersonic combustion flow paths. *Shock Waves* **20**, 353–366.

Hannemann, K., Schnieder, M., Reimann, B. & Schramm, J. Martinez 2000 The influence and delay of driver-gas contamination in HEG. AIAA Paper No. 2000-2593, June 2000.

Hannemann, K., Schramm, J. Martinez, Karl, S. & Steelant, J. 2008 Experimental investigation of different scramjet hydrogen injection systems. In *Proc. 6th European Symposium on Aerothermodynamics for Space Vehicles*. Versailles, France.

Heiser, W.H. & Pratt, D.T. 1994 *Hypersonic airbreathing propulsion*. AIAA Education Series, AIAA, Washington, DC.

Herning, F. & Zipperer, L. 1936 Beitrag zur Berechnung der Zähigkeit technischer Gasgemische aus den Zähigkeitswerten der Einzelbestandteile. *Das Gas- und Wasserfach* **4**, 69–73.

Jameson, A. 1991 Time dependent calculations using multigrid, with application to unsteady flows past airfoils and wings. AIAA Paper No. 91-1596, 1991.

Karl, S. 2011 Numerical investigation of a generic scramjet configuration. PhD thesis, Technische Universität Dresden, Dresden, Germany.

Karl, S. & Hannemann, K. 2008 CFD analysis of the HyShot II scramjet experiments in the HEG shock tunnel. AIAA Paper No. 2008-2548, April 2008.

Korkegi, R.H. 1975 Comparison of shock induced two and three-dimensional incipient turbulent separation. *AIAA J.* **13** (4), 534–535.

Love, E.S. 1955 Pressure rise associated with shock-induced boundary-layer separation. NACA TN D-3601.

Matsuo, K., Miyazato, Y. & Kim, H.-D. 1999 Shock train and pseudo-shock phenomena in internal gas flows. *Prog. Aerosp. Sci.* **35**, 33–100.

McDaniel, K.S. & Edwards, J.R. 1999 Simulation of thermal choking in a model scramjet combustor. AIAA Paper No. 99-3411, June 1999.

McDaniel, K.S. & Edwards, J.R. 2001 Three-dimensional simulation of thermal choking in a model scramjet combustor. AIAA Paper No. 2001-0382, Jan. 2001.

Newsome, R.W. 1984 Numerical simulation of near-critical and unsteady, subcritical inlet flow. *AIAA J.* **22** (10), 1375–1379.

O'Byrne, S., Doolan, M., Olsen, S. R. & Houwing, A. F. P. 2000 Transient thermal choking processes in a model scramjet engine. *J. Prop. Power* **16** (5), 808–814.

Rodi, P.E., Emami, S. & Trexler, C.A. 1996 Unsteady pressure behaviour in a ramjet/scramjet inlet. *J. Prop. Power* **12** (3), 486–493.

Settles, G.S. 2006 *Schlieren and shadowgraph techniques*. Springer, NY.

Shapiro, A.H. 1953 *The dynamics and thermodynamics of compressible fluid flow*. The Ronald Press Company, NY.

Shimura, T., Mitani, T., Sakuranaka, N. & Izumikawa, M. 1998 Load oscillations caused by unstart of hypersonic wind tunnels and engines. *J. Prop. Power* **14** (3), 348–353.

Smart, M.K., Hass, N.E. & Paull, A. 2006 Flight data analysis of the Hyshot 2 scramjet flight experiment. *AIAA J.* **44** (10), 2366–2375.

Tan, H.-J. & Guo, R.W. 2007 Experimental study of the unstable-unstarted condition of a hypersonic inlet at mach 6. *J. Prop. Power* **23** (4), 783–788.

Tan, H.-J., Li, L.G., Wen, Y.-F. & Zhang, Q.-F. 2011 Experimental investigation of the unstart process of a generic hypersonic inlet. *AIAA J.* **49** (2), 279–288.

Wagner, J. L., Yuceil, K. B., Valdivia, A., Clemens, N.T. & Dolling, D.S. 2009 Experimental investigation of unstart in an inlet/isolator model in Mach 5 flow. *AIAA J.* **47** (6), 1528–1542.

Wieting, A.R. 1976 Exploratory study of transient unstart phenomena in a three-dimensional fixed-geometry scramjet engine. NASA TN D-8156.

Wilke, C.R. 1950 A viscosity equation for gas mixtures. *J. Chem. Phys.* **18** (4), 517–519.